Article

MJF-14 proximity ligation assay detects early non-inclusion alpha-synuclein pathology with enhanced specificity and sensitivity

Check for updates

Nanna Møller Jensen [1,2] ✉, YuHong Fu [3], Cristine Betzer[1,2], Hongyun Li[3], Sara Elfarrash [1,2,8], Ali H. Shaib[4], Donatus Krah[4], Zagorka Vitic[1,2], Lasse Reimer[1,2], Hjalte Gram[1,2], Vladimir Buchman[5], Mark Denham[1,2], Silvio O. Rizzoli[4,6], Glenda M. Halliday [3,7] & Poul Henning Jensen [1,2] ✉

α-Synuclein proximity ligation assay (PLA) has proved a sensitive technique for detection of non-Lewy body α-synuclein aggregate pathology. Here, we describe the MJF-14 PLA, a new PLA towards aggregated α-synuclein with unprecedented specificity, using the aggregate-selective α-synuclein antibody MJFR-14-6-4-2 (hereafter MJF-14). Signal in the assay correlates with α-synuclein aggregation in cell culture and human neurons, induced by α-synuclein overexpression or pre-formed fibrils. Co-labelling of MJF-14 PLA and pS129-α-synuclein immunofluorescence in post-mortem cases of dementia with Lewy bodies shows that while the MJF-14 PLA reveals extensive non-inclusion pathology, it is not sensitive towards pS129-α-synuclein-positive Lewy bodies. In Parkinson's disease brain, direct comparison of PLA and immunohistochemistry with the MJF-14 antibody shows widespread α-synuclein pathology preceding the formation of conventional Lewy pathology. In conclusion, we introduce an improved α-synuclein aggregate PLA to uncover abundant non-inclusion pathology, which deserves future validation with brain bank resources and in different synucleinopathies.

Synucleinopathies are a group of neurological diseases with proteinaceous inclusions, denoted Lewy bodies (LBs) and Lewy neurites, as the histopathological hallmark. Since the identification of aggregated α-synuclein as a primary constituent of these inclusions, researchers have sought to elucidate the exact involvement of α-synuclein aggregates in the pathogenesis of these diseases. Comprising Parkinson's disease (PD), dementia with Lewy bodies (DLB), and multiple system atrophy (MSA) as the most prominent, the synucleinopathies are principally age-related neurodegenerative diseases[1–3]. Although the majority of cases are sporadic, specific mutations and multiplications of the SNCA gene cause familial PD, underscoring the importance of α-synuclein in the pathogenesis[4–9]. In certain conditions, α-synuclein readily misfolds and accumulates into various aggregates; first the small soluble oligomers and later the larger, insoluble fibrils, which can then associate with other cellular components and form LBs[10–12]. Mapping of Lewy pathology in PD patients with variable disease duration has revealed distinct patterns of pathology in the central nervous system, leading to the prion-like spreading hypothesis[13–16] and one of the current classifications of disease severity: the Braak staging[17,18].

Though the LBs are striking markers of synucleinopathies, it has long been contested whether the LBs actually cause neuronal death and confer the spreading of pathology between cells—or whether they instead represent either a protective cellular response sequestering aberrant α-synuclein or simply an epiphenomenon[11,19–23]. As a consequence, attention has fallen upon the α-synuclein oligomers, which are much smaller, soluble structures

[1]DANDRITE - Danish Research Institute of Translational Neuroscience, Aarhus C, Denmark. [2]Department of Biomedicine, Aarhus University, Aarhus C, Denmark. [3]Brain and Mind Centre & Faculty of Medicine and Health, School of Medical Sciences, University of Sydney, Camperdown, NSW, Australia. [4]Department of Neuro- and Sensory Physiology, University Medical Center Göttingen, Göttingen, Germany. [5]School of Biosciences, Cardiff University, Cardiff, UK. [6]Center for Biostructural Imaging of Neurodegeneration (BIN), Göttingen, Germany. [7]Neuroscience Research Australia & Faculty of Medicine, School of Medical Sciences, University of New South Wales, Sydney, NSW, Australia. [8]Present address: Department of Physiology, Faculty of Medicine, Mansoura University, Mansoura, Egypt. ✉e-mail: nanna.mj@biomed.au.dk; phj@biomed.au.dk

formed during the aggregation process[24-33]. Oligomers are thus hypothesised to be a major culprit in both disease symptomatology and progression of synucleinopathies—as well as a potential therapeutic target[34-40]. However, detecting oligomeric structures is challenging, perhaps due to factors such as smaller size and more transient, ill-defined conformations. In standard immunohistochemistry, the potential presence of oligomers is overshadowed by the presence of abundant native α-synuclein and the much larger, intensely stained LBs and Lewy neurites, even using aggregate-specific or -selective antibodies[32]. Furthermore, though antibodies with oligomer-preference have been reported, there are currently no antibodies capable of distinguishing between oligomeric and fibrillar α-synuclein[41,42].

As an alternative to the aggregate-specific immunohistochemistry, proximity-dependent strategies have been employed to detect oligomers, including the bimolecular fluorescence complementation assay (BiFC) and the proximity ligation assay (PLA). Where the BiFC utilises a proximity-dependent completion of a fluorophore to detect the early stages of α-synuclein aggregation[43,44], the PLA relies on antibody-based binding of proximity probes within approximately 40 nm, followed by a signal amplification to achieve high sensitivity[45]. In 2015, using the syn211 antibody against total α-synuclein, Roberts et al. demonstrated a preferential staining of in vitro-generated oligomers over both fibrils and monomeric α-synuclein in the so far predominant α-synuclein PLA. When used in PD patient tissue, the PLA mainly stained early-stage pathology preceding the LBs, such as pale bodies[46]. The use of a total α-synuclein-antibody, however, can pose an issue, especially in settings where α-synuclein expression is increased, as the PLA in itself does not preclude the detection of closely located monomers of the protein, e.g., when bound to cellular vesicles.

In this paper, we describe the development of a new α-synuclein PLA with excellent detection of non-inclusion pathology, i.e., α-synuclein aggregates that are not organised into LBs or Lewy neurites. Specificity in the assay is obtained by the utilisation of conformation-specific antibody MJFR-14-6-4-2 (MJF-14) towards aggregated α-synuclein[47,48]. We directly demonstrate this specificity in a cell model overexpressing α-synuclein, in conditions with and without α-synuclein aggregation, and compare it against the existing syn211 PLA. Furthermore, we characterise the usability of the MJF-14 PLA, both in fluorescent and chromogenic applications, in cultured human cortical neurons, post-mortem brain tissue of PD and DLB, and in mouse models of synucleinopathies. Lastly, we describe the development of a machine-learning-based automated segmentation and quantification of chromogenic PLA, enabling large-scale quantification studies.

Results
Development of an α-synuclein aggregation-specific proximity ligation assay
Proximity ligation is based on the antibody-facilitated detection of two targets in close proximity, whereby signal amplification allows visualisation of each individual proximity interaction (Fig. 1a). Thus, the choice of antibodies becomes crucial in determining which targets are detected. As α-synuclein overexpression models are regularly used in synucleinopathy research, we speculated that PLAs utilising antibodies binding total α-synuclein might be suboptimal due to potential detection of closely located native monomeric α-synuclein species in the overexpression systems, e.g., associated to membrane surfaces. We hypothesised that using an antibody targeting aggregated α-synuclein would give a higher specificity of the PLA towards α-synuclein aggregates. To test the hypothesis, we used Tet-off SNCA transgenic human neuroblastoma cells (SH-SY5Y AS), in which α-synuclein overexpression in non-mitotic differentiated cells is induced by the removal of doxycycline, leading to the development of α-synuclein aggregates[49,50]. In addition to setting up conditions with and without α-synuclein expression (±doxycycline), in some cultures, α-synuclein aggregation inhibitor ASI1D[51] was added to prevent aggregation of the expressed α-synuclein (Fig. 1b). Then, PLA was conducted using either the total α-synuclein antibody syn211, as has previously been published[46,52-54], or the aggregate-sensitive α-synuclein antibody MJF-14, which preferentially detects pathologically misfolded α-synuclein[47,48].
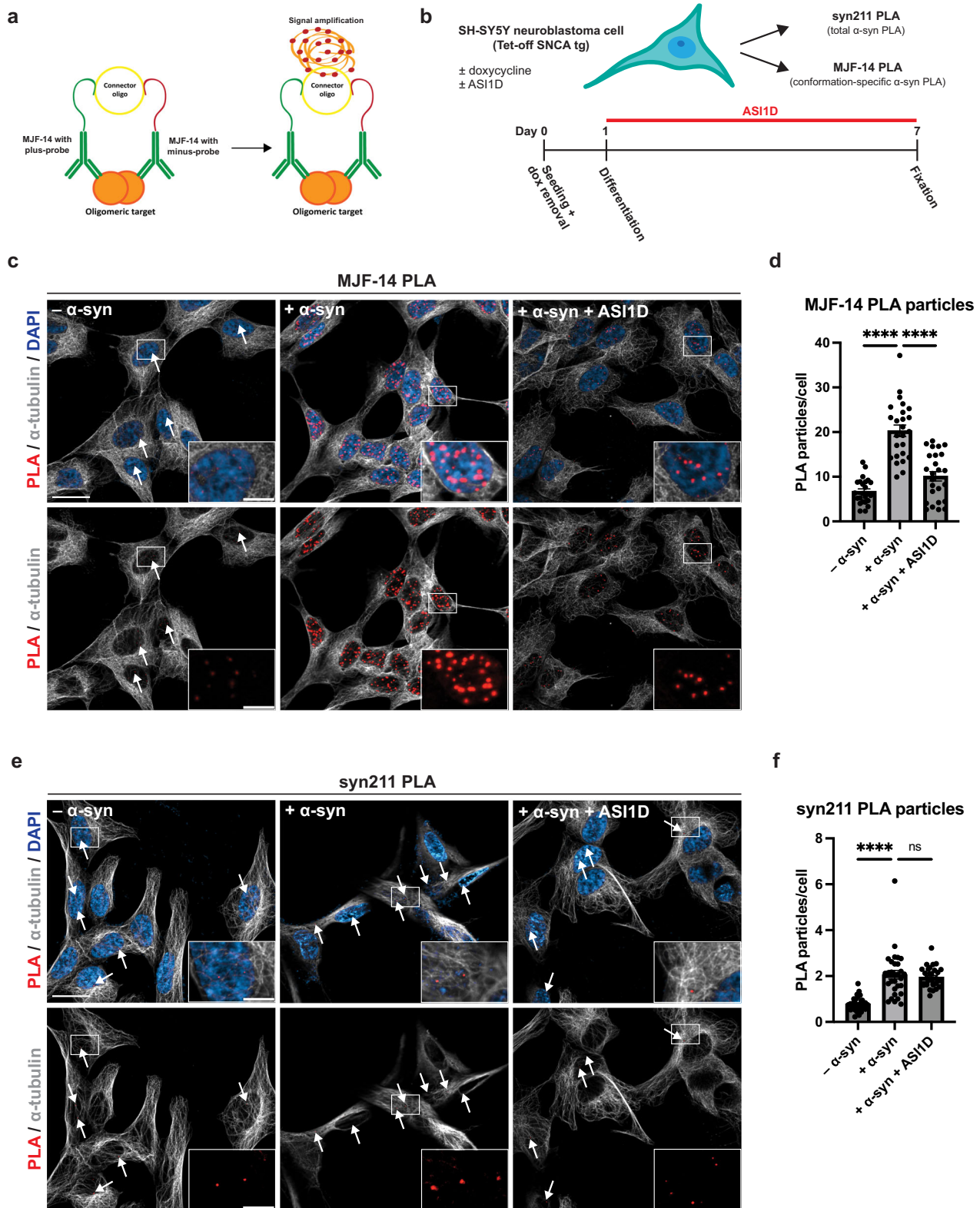
In conditions without α-synuclein overexpression, only a small amount of MJF-14 PLA signal was detected, while α-synuclein-overexpressing cultures contained widespread signal (Fig. 1c, d). Technical negative controls (PLA without ligase in the reaction) were included in all experiments, and their lack of signal for both antibodies ensured the functionality of the assay (Supplementary Fig. 1a). When the α-synuclein aggregate inhibitor ASI1D was added to the α-synuclein overexpressing cells, the MJF-14 PLA signal was returned almost to the same level as without α-synuclein overexpression (Fig. 1c, d). Notably, there were not only significantly more PLA particles in α-synuclein-overexpressing cultures than when treated with ASI1D or without α-synuclein overexpression, the particles were also significantly brighter (Fig. 1c, insets). A likely cause for this phenomenon is the presence of multiple rolling circle amplification products in such a close vicinity that they coalesce in imaging, i.e., probably located on the same aggregate. Because of this potential coalescing of particles, it might in some cases be more suitable to quantify either PLA particle area or integrated density (i.e., intensity times area), which can lead to a greater distinction between conditions (Supplementary Fig. 1b). Of note, we did observe some differences in the MJF-14 PLA signal levels between biological replicates (see PLA particle counts in Fig. 1d and Supplementary Fig. 1b), coinciding with differences in α-synuclein expression levels between batches of cells. The overall pattern of increased MJF-14 PLA signal upon α-synuclein overexpression and a decrease in signal with ASI1D treatment was consistent across replicates.

The syn211 PLA performed on parallel cultures also displayed an increase in PLA signal when α-synuclein overexpression was turned on. Syn211 PLA signal, however, was not reduced by ASI1D treatment, indicating that the syn211 PLA signal was not aggregation-dependent (Fig. 1e, f). In general, the signal from the syn211 PLA was much lower than that from the MJF-14 PLA in all conditions, despite an increased antibody concentration (1:100 compared to 1:750 as previously published for fluorescent syn211 PLA) and efforts to optimise amplification time. This indicates that the MJF-14 PLA could be more sensitive towards very early types of aggregates. Collectively, we found that aggregation of α-synuclein is necessary for the generation of MJF-14 PLA signal, whereas the syn211 PLA may recognise physiological clustering as demonstrated, e.g., on surfaces of vesicles[55-58]. Hence, we decided to further characterise the PLA based on the use of the MJF-14 antibody.

MJF-14 PLA detects PFF-seeded pathology in human cortical neurons
To further investigate the usability of the MJF-14 PLA in PD model systems, we next cultured human cortical neurons in chambered slides. Pathology was induced by addition of pre-formed fibrils (PFFs) of recombinant human α-synuclein, which cause the endogenous α-synuclein in the neurons to aggregate upon contact[59]. As the MJF-14 antibody recognises an epitope present across aggregate types from oligomers to fibrils, including in the PFFs[42,47,48], we speculated that there might be some detection of the added PFFs when performing PLA on PFF-treated cultures. Neurons were therefore treated with either full-length S129A-mutated PFFs or the recently described AS-141G PFFs (S129A-mutated α-synuclein-141G), which are invisible to the MJF-14 antibody due to a C-terminally added glycine[60]. Both types of PFFs were S129A-mutated to allow the usage of pS129-α-synuclein immunostaining to simultaneously visualise S129 phosphorylation without any risk of staining in cellulo phosphorylations on the added PFFs.

To assess both the ability of the PFFs to induce α-synuclein aggregate pathology and any potential detection of the added PFFs, cultures were fixed at two different timepoints (Fig. 2a). At 2 h post treatment, any signal above background levels in the cultures should stem from direct detection of the added PFFs and, indeed, S129A PFF-treated cultures showed increased PLA signal ($p < 0.0001$, Fig. 2b, c). Signal in AS-141G PFF cultures, though, was not significantly different from the background level seen in PBS-treated cultures ($p = 0.2318$), indicating that the AS-141G PFFs were not detected in the PLA. We also performed IF on some of the cultures, using the MJF-14 antibody and the LB509 antibody towards total human α-synuclein. MJF-14

a

b SH-SY5Y neuroblastoma cell (Tet-off SNCA tg)

syn211 PLA (total α-syn PLA)

MJF-14 PLA (conformation-specific α-syn PLA)

± doxycycline ± ASI1D

c MJF-14 PLA

d MJF-14 PLA particles

e syn211 PLA

f syn211 PLA particles

IF signal was vastly increased in S129A PFF-treated cultures, corresponding to the detection of these PFFs, while no signal was observed in PBS- or AS-141G PFF-treated cultures (Supplementary Fig. 2a). Total α-synuclein staining, which will detect both the endogenous α-synuclein but also any PFFs, whether intracellular or extracellular, showed similar, increased levels for both types of PFFs (Supplementary Fig. 2a). Most of the LB509 staining in the S129A PFF-treated cultures was co-localised with the MJF-14

staining, indicating that the increased α-synuclein staining was mostly due to the PFFs. Staining for pS129-α-synuclein did not show any substantial signal at 2 h post treatment, which was to be expected as both types of PFFs were S129A-mutated (Fig. 2b).

7 days after PFF treatment, internalised PFFs should have templated the aggregation of endogenous α-synuclein in the neurons, while the PFFs themselves should be mostly truncated C-terminally[61–63]. As the epitope for

Fig. 1 | MJF-14 PLA signal is directly dependent upon aggregate formation in α-synuclein transgenic neuroblastoma cells. a Principle of the proximity ligation assay for detection of α-synuclein aggregates. **b** Experimental setup: α-synuclein transgenic SH-SY5Y cells are differentiated into non-mitotic neuronal-like cells using retinoic acid, treated ± doxycycline to mediate α-synuclein overexpression and ± ASI1D to modulate α-synuclein aggregation. Then, cells are fixed and subjected to PLA using the α-synuclein conformation-specific MJFR-14-6-4-2 antibody or the total α-synuclein syn211 antibody. **c** Representative images of MJF-14 PLA in conditions without α-synuclein expression, with α-synuclein expression, and with α-synuclein expression + ASI1D-treatment. PLA signal is displayed in red (small dots), α-tubulin in grey and DAPI in blue. Arrows indicate examples of PLA particles in low abundance conditions. Scale bar = 20 μm. **d** Quantification of the number of PLA particles per cell, as determined by the MJF-14 PLA. The +α-syn condition is significantly different from both -α-syn and +α-syn + ASI1D ($p < 0.0001$). **e** Representative images of syn211 PLA in conditions without α-synuclein expression, with α-synuclein expression, and with α-synuclein expression + ASI1D-treatment. PLA signal is displayed in red (small dots), α-tubulin in grey and DAPI in blue. Arrows indicate examples of PLA particles in low abundance conditions. Scale bar = 20 μm. **f** Quantification of the number of PLA particles per cell, as determined by the syn211 PLA. The +α-syn condition is significantly different from -α-syn ($p < 0.0001$) but not +α-syn + ASI1D ($p > 0.9999$). Graphs display mean ± SEM from one replicate and each dot signifies one image. Experiments were performed minimum three times independently, and groups were compared using a Kruskal-Wallis one-way ANOVA followed by the Dunn post hoc test. ****$p < 0.0001$.

the MJF-14 antibody is formed by the last four residues in the α-synuclein protein, the truncated PFFs will be invisible to the MJF-14 antibody[60,64]. Thus, MJF-14 PLA signal present after 7 days stems from the aggregation of endogenous α-synuclein in the cultures, which was seen at similar levels after either S129A or AS-141G PFF treatment (Fig. 2d, e). This was further supported by IF detection of increased α-synuclein deposition following either PFF treatment, based on both pS129-α-synuclein (Fig. 2d) and MJF-14 IF (Supplementary Fig. 2b). Interestingly, although there was some co-detection of α-synuclein species by both the MJF-14 PLA and the pS129-α-synuclein IF, the two staining techniques also labelled distinct species, highlighting a discrepancy between phosphorylation and aggregation (Fig. 2d, f). We also observed that while α-synuclein accumulation into brightly fluorescent deposits was detected by MJF-14 IF after both PFF treatments, the signal-to-noise ratio was much higher in AS-141G PFF cultures (Supplementary Fig. 2b). This could indicate that a fraction of the full-length S129A PFFs is still present, perhaps bound to the extracellular surface of the neurons, and thereby cause background staining.

Taken together, we show that the MJF-14 PLA can detect PFF-induced α-synuclein pathology with either type of PFF tested here but that it also has some detection of added full-length S129A PFFs, especially at early time-points. This challenge can be largely avoided by the use of AS-141G PFFs, which are invisible to the MJF-14 antibody and yield increased signal-to-noise ratio for both the MJF-14 PLA and MJF-14 IF.

MJF-14 PLA reveals extensive non-Lewy body pathology in DLB brain samples

To further explore the MJF-14 PLA and its ability to stain synucleinopathy-related pathology, we studied sections of the superior frontal cortex from patients with DLB and from brains without identified neurodegenerative disease. The sections were stained with the MJF-14 PLA in its fluorescent mode (red label) followed by a traditional immunofluorescence staining for pS129-α-synuclein (grey) to detect conventional LB pathology. Initial staining of both DLB and control brain sections revealed substantial fluorescence in the red channel, regardless of performing the PLA reaction with or without the antibodies added, and with or without the ligase in the PLA reaction (Fig. 3a). Most likely, the cause was lipofuscin-related autofluorescence, as described for human brain samples[65,66]. Thus, an autofluorescence quenching step using TrueBlack was introduced, which efficiently suppressed autofluorescence and left the technical negative controls (PLA minus antibody and PLA minus ligase) void of signal (Fig. 3b).

Following autofluorescence quenching, MJF-14 PLA-staining revealed considerable pathology in DLB brains, while control brains contained some PLA-staining, but at significantly lower levels as demonstrated by lower area covered by PLA per image (Fig. 3c, d). The level of PLA signal in non-neurodegenerative control brain was similar to what has previously been reported for the syn211 PLA on non-neurodegenerative controls by Roberts et al.[46]. Of note, the appearance of the MJF-14 PLA signal (Fig. 3c) and the lipofuscin-related autofluorescence (Fig. 3a) was very similar, based on morphology, abundance, and localisation. Thus, proper technical controls are critical to ensure the specificity of the observed signal. Here, our

TrueBlack technical negative controls (without any signal; Fig. 3b) were stained and imaged in parallel with the PLA-stained cases in Fig. 3c, using the same imaging and processing settings, which ensured that the signal under these conditions was dependent on the specific PLA reaction.

In the DLB cases, PLA-staining was found both in neurons with and without LBs, but there was only very sparse, if any, PLA-staining of the pS129-labelled LBs in the cases analysed (Fig. 3e). As the MJF-14 antibody does recognise LBs in IHC (see Fig. 4a), the inability of the MJF-14 PLA to efficiently label LBs is not antibody-related. Rather, the lack of PLA signal might indicate a structural organisation of α-synuclein aggregates in LBs that differs from the MJF-14 PLA-positive non-inclusion aggregates and does not allow the necessary signal amplification in the PLA. A closer look at the PLA particles showed there was a weak pS129-labelling of these particles (Fig. 3e, smaller panels), demonstrating that co-labelling of aggregates with MJF-14 PLA and pS129 IF is not generally incompatible.

PD brains display significant MJF-14 PLA signal even at early stages

To confirm that the PLA results were not limited to IF and reduce the likelihood of mistaking age-related lipofuscin for the PLA signal, we also tested the MJF-14 PLA using a chromogenic detection system. For this, we employed a cohort of Braak stage IV and VI PD patients and non-neurodegenerative controls (Table 1). We selected the anterior cingulate cortex as our target region, as stage IV and VI PD patients are easily distinguishable by their Lewy pathology in this region (LBs are present in stage VI PD, but only rarely in stage IV PD)[67]. A comparison of the MJF-14 PLA with MJF-14 IHC on neighbouring sections clearly demonstrated the difference in specificity between IHC and PLA. Where IHC preferentially detected LBs, the PLA uncovered abundant non-inclusion pathology distributed throughout the tissue of PD patients (Fig. 4a).

A disadvantage of chromogenic staining is the difficulty it poses in attempts to properly quantify pathology, as signals are not simply separated in different wavelength channels as for immunofluorescence. Instead, the image consists of many compound signals, which need to be separated before quantification. To do this, we employed a machine-learning based technique, the open-source Trainable Weka Segmentation in Fiji[68], to train a classifier, perform automated segmentation, and subsequently analyse the PLA-density in the sections (Supplementary Fig. 4).

Initially, we found striking PLA signal in PD, with no difference between stage IV and VI PD ($p = 0.551$). Both groups, however, were easily distinguished from the controls, which only contained very low levels of PLA signal ($p < 0.001$; Fig. 4b). As a comparison, we also quantified the MJF-14 IHC signal in the three groups, in the form of (i) deposit particles (any MJF-14 signal with a minimum length of 2 μm and intensity >50 above background, automated quantification) and (ii) LBs specifically (round or oval-shaped, minimum 5 μm in diameter, sometimes with a halo, counted manually by two independent researchers). As expected from the group selection criteria, MJF-14 IHC was not able to discriminate stage IV PD from controls by any of the two measures ($p = 0.093$ and $p = 0.169$, respectively; Fig. 4c, d). The stage VI PD group, though, was easily distinguishable from both controls ($p < 0.001$) and stage IV PD ($p = 0.011$ and
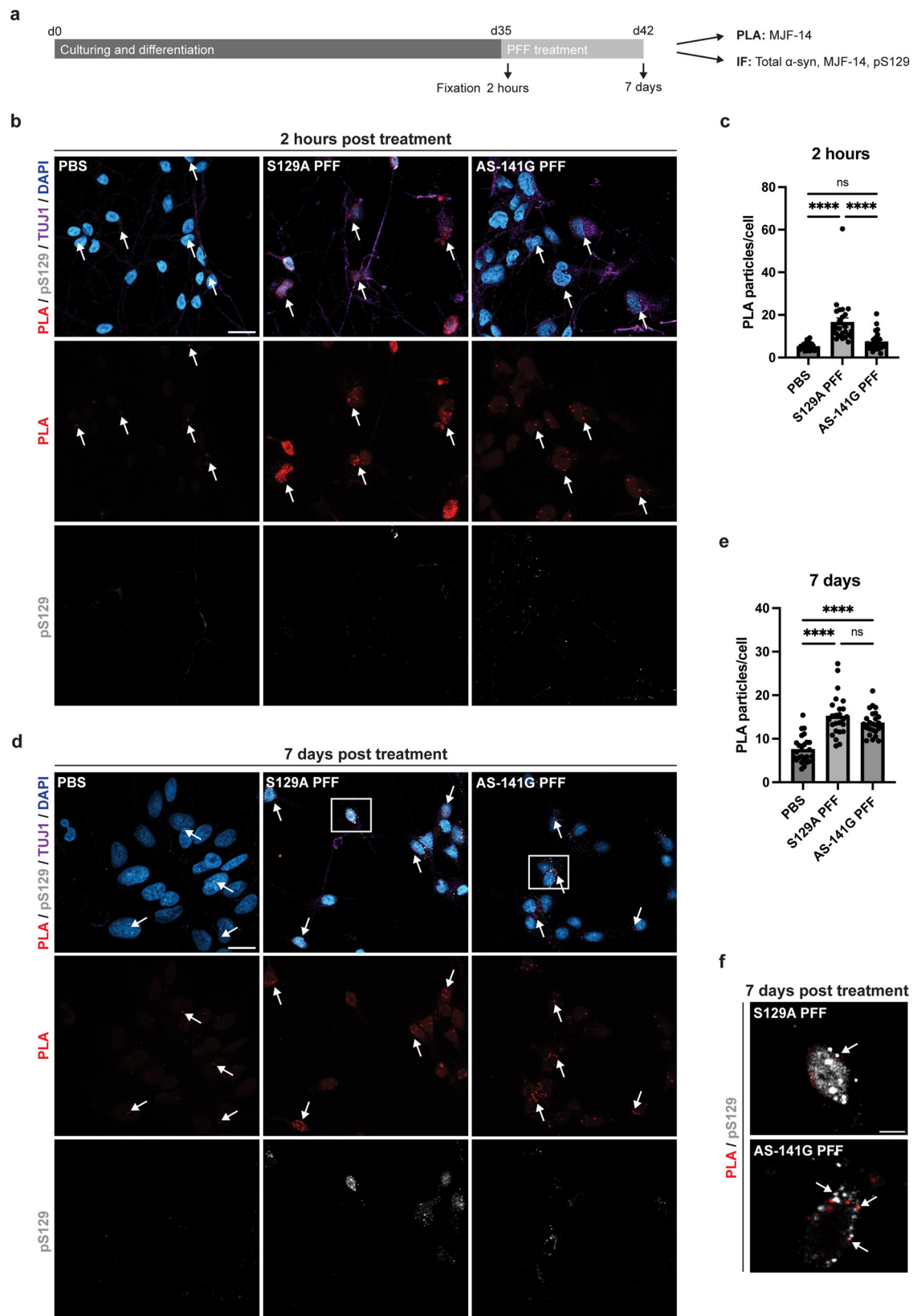
$p < 0.001$), based on either deposit particles (Fig. 4c) or LBs (Fig. 4d). Mean and SEM values depicted in Fig. 4b–d can be found in Suppl. Table 4. In stage VI, it was evident that the LBs were selectively accumulated in the deep layers of the ACC ($p < 0.001$), as has previously been reported[11,18,69]. We did not, however, detect any differences in PLA distribution between the superficial (SGM) and deep (DGM) layers of the ACC, nor any interaction between group and region. Between the cases, we observed some variation in the nuclear counterstain on the PLA-stained sections, though both intense and weak counterstain could be found in each group and with both high and low PLA signal levels (Supplementary Fig. 3, Supplementary Table 3). There

Fig. 2 | AS-141G PFFs induce formation of PLA signal in human neurons but added PFFs themselves are undetected. a Human cortical neurons were cultured for 35 days before treatment with either S129A PFFs, AS-141G PFFs (S129A-α-synuclein-141G), or PBS, and fixed after 2 h or 7 days. **b** Representative images from 2 h post treatment cultures immunostained with MJF-14 PLA (red), pS129-α-synuclein (grey), βIII-tubulin/TUJ1 (purple), and DAPI nuclear stain (blue). Arrows indicate examples of PLA signals. Scale bar = 20 μm. **c** Quantification of the number of PLA particles per cell after 2 h, as determined by the MJF-14 PLA. Treatment significantly affects PLA signal density (F(2,269) = [47.79], $p < 0.0001$), with the S129A PFF group differing from both PBS and AS-141G PFF groups ($p < 0.0001$) while PBS and AS-141G PFF groups do no differ significantly ($p = 0.2318$). **d** Representative images from 7 days post treatment cultures immunostained with MJF-14 PLA (red), pS129-α-synuclein (grey), βIII-tubulin (purple), and DAPI

nuclear stain (blue). Arrows indicate examples of PLA signals. Scale bar = 20 μm. **e** Quantification of the number of PLA particles per cell after 7 days, as determined by the MJF-14 PLA. Treatment significantly affects PLA signal density (F(2,296) = [35.26], $p < 0.0001$), with the PBS group differing from both S129A and AS-141G PFF groups ($p < 0.0001$) while S129A and AS-141G PFF groups do no differ significantly ($p = 0.5009$). **f** Magnified panels from (**d**) with arrows indicating the co-detection of particles with both MJF-14 PLA (red) and pS129-α-synuclein (grey). Scale bar = 5 μm. Graphs display mean ± SEM from two independent replicates and each dot signifies one image. Experiments were performed two times independently with two technical replicates each time, and groups were compared using a two-way ANOVA followed by Tukey's multiple comparison test. ****$p < 0.0001$.

was no obvious correlation between the intensity of the counterstain and any of the covariates in our analyses, nor cause of death in the cohort (Supplementary Table 2). Likewise, cause of death did not appear to directly affect PLA signal density in the cases (Supplementary Tables 2, 3).

Further investigation of the stage VI PD group—in which there were substantial amounts of PLA signal, IHC deposit particles, and LBs—revealed an inverse logarithmic correlation between PLA particle density and IHC deposit particle density (Fig. 4f). In addition, we detected a positive logarithmic correlation between IHC deposit particle and LB density (Fig. 4g), but no direct correlation between PLA signal and LB density (data not shown). Thus, the patients with the lowest density of PLA particles were the ones in which the highest density of IHC deposit particles was found, in contrast to the findings by Roberts et al. in the cingulate cortex[46]. This suggests that the MJF-14 PLA signal indeed represents early α-synuclein pathology, which may be sequestered into early types of deposits detected by IHC and later matures into LBs. To test this hypothesis, we revisited some of the DLB tissue stained for both MJF-14 PLA and pS129 (Fig. 3) and did a direct comparison of PLA signal in LB-positive and neighbouring LB-negative large neurons. Intriguingly, the average PLA area was 36% higher in LB-negative than LB-positive large neurons, supporting a process where PLA-positive aggregates could be sequestered into inclusions (Supplementary Fig. 5).

We also looked further into the distribution of PLA signal between neuronal cell bodies and the neuropil (see Fig. 4h and methods for segmentation definition). Overall, there was a strong linear correlation between neuronal and neuropil PLA with R = 0.938 ($p < 0.001$), and around 30% of the total PLA particles were localised in neuronal cell bodies, i.e., in nuclei or surrounding cytoplasm (33.6% for PD stage IV and 28.9% for PD stage VI, Supplementary Table 7). Thus, the majority of the PLA signal was located away from the neuronal nuclei, in what is here denoted neuropil but also comprises axons, dendrites, and extra-neuronal matrix including various glial cells. A prime candidate for its principal location is the presynaptic and axonal compartments, which are believed to be the earliest affected parts of the neurons[64,70–73].

Looking to the neuronal cell bodies, 6.76% of the neurons in controls contained PLA signal, while this proportion was almost 10-fold higher in PD, with 70.5% in stage IV PD and 63.5% in stage VI PD (Fig. 4e and Suppl. Table 5). Particularly in the stage VI PD group, there was a considerable variation in the fraction of PLA-positive neurons between cases, indicating a heterogeneity not accounted for by the Braak staging. In addition to the higher proportion of PLA-positive neurons in the PD groups, the average load of PLA in affected neurons was also increased in the PD groups (Fig. 4i, j and Supplementary Table 6). The proportion of PLA-containing neurons was also much higher than the corresponding proportions containing deposit particles in general (approx. 4.7% in stage IV and 10.7% in stage VI PD) or LBs specifically (4.13% in stage VI PD; Supplementary Table 5). There was no significant difference in the number of neurons per region of interest between the three groups ($p = 0.103$). Taken together, this demonstrates that the MJF-14 PLA can reveal an unappreciated level of pathology in the tissue, affecting around 15 times as many neurons as the LBs do.

To appraise whether the PLA particles accumulated in a specific part of the neurons and if this changed with Braak stage, we did a semi-quantitative single-neuron analysis, assessing PLA distribution between nuclear and cytosolic compartments. This revealed that most of PLA-containing neurons in both PD groups had signal either solely in the cytoplasm or in both nucleus and cytoplasm (Fig. 4k, Supplementary Table 7). The mixed distribution (PLA particles in both nucleus and cytoplasm) was highly specific for PD and did not occur in controls. We did not, however, find any obvious differences in the PLA distribution (nuclear vs. cytosolic) between neurons in stage IV and VI PD in the ACC, which could inform on the subcellular origin of the PLA particles. A potential explanation for the lack of differences in the PLA distribution between the two PD groups could be that the PLA signal has already been saturated in this region at Braak stage IV. Consequently, it may be necessary to look at even earlier disease stages or different regions to investigate the origin of the PLA particles. Still, our results underscore the potential of single-neuron PLA analysis as a supplement to the previously seen semi-quantitative general tissue scoring methods.

A fraction of neuropil MJF-14 PLA signal localises to the pre-synaptic terminal

Following our observations on the PD cohort in the anterior cingulate cortex, leading to the realisation that the majority of PLA signal is located in the neuropil, we wanted to explore the exact localisation of these neuropil PLA signals. As the structures in the neuropil and the PLA signals themselves are quite small, the diffraction limit can significantly restrict our ability to demonstrate a true co-localisation. Therefore, we set out to combine our PLA protocol with one-step nanoscale expansion (ONE) microscopy[74] to push the resolution as far as possible (Fig. 5a). Since the choice of fluorophores is a crucial factor in expansion microscopy, we switched to a custom-made PLA kit from Navinci for the ONE microscopy, which allowed labelling with multiple different fluorophores depending on our need. For non-expansion experiments, standard Navinci detection reagents were used (both chromogenic and fluorescent).

From one of our DLB cases, we had motor cortex sections available, which we could use to study the neuropil PLA signal and compare it with motor cortex from a non-neurodegenerative control. Initial chromogenic PLA staining was performed to (i) compare the MJF-14 PLA from Duolink and Navinci and (ii) to form an impression of the PLA signal distribution in these cases for the following expansion experiments. Overall, MJF-14 PLA staining using kits from Duolink and Navinci resulted in similar staining patterns, with some parts of the DLB motor cortex mainly containing neuropil PLA, while other parts mainly showed PLA in the cell body, both nuclear and cytoplasmic (Supplementary Fig. 6a, top). The non-neurodegenerative control motor cortex was virtually blank with both company kits (Supplementary Fig. 6a, bottom). On closer inspection, we observed a strong labelling of what appeared to be LBs/inclusions with the Navinci MJF-14 PLA, which were not found with the Duolink MJF-14 PLA (Supplementary Fig. 6a). Fluorescent application of the Navinci MJF-14 PLA combined with pS129 IF confirmed that the pS129-positive LBs were indeed labelled by this PLA kit (Supplementary Fig. 6b). This indicates that not only epitope presentation in the aggregates but also the company-
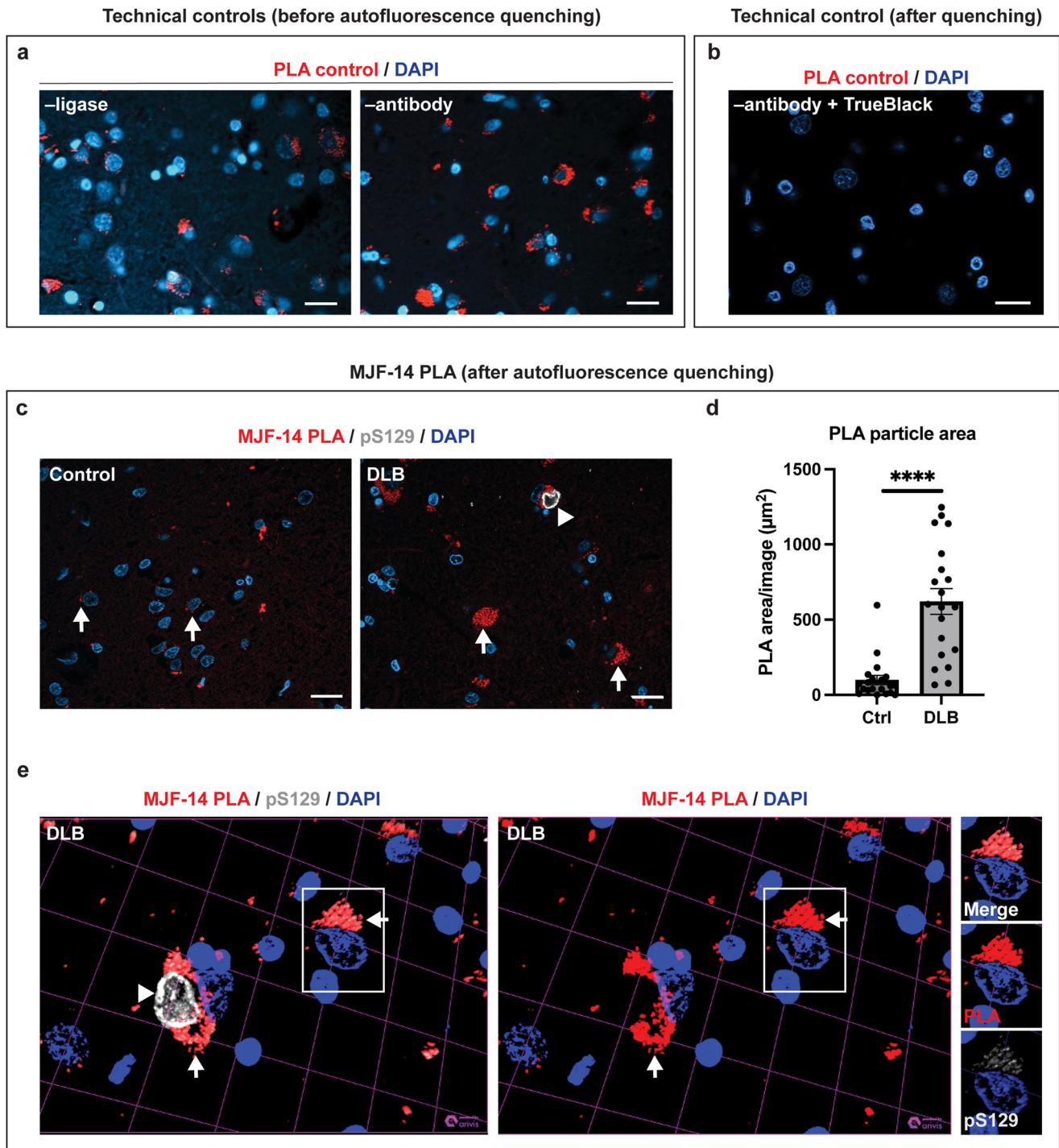
Technical controls (before autofluorescence quenching)

Technical control (after quenching)

MJF-14 PLA (after autofluorescence quenching)

Fig. 3 | MJF-14 PLA stains considerable pathology in DLB brains but is not sensitive to Lewy bodies. a Technical negative controls: PLA –ligase in the reaction (left) and PLA –antibody (right) display significant amounts of red channel signal when autofluorescence is not quenched. Scale bars = 20 μm. **b** TrueBlack-quenching of autofluorescence effectively removes background signal in technical negative controls (here, PLA –antibody). Scale bar = 20 μm. **c** Representative images of sections immunostained with MJF-14 PLA (red), pS129-α-synuclein (pS129, grey), and DAPI nuclear stain (blue) in control (left) and DLB (right). Examples of PLA-positive neurons are indicated with arrows, while a LB-positive neuron is indicated by an arrowhead. Scale bars = 20 μm. **d** Quantification of PLA particle area in control and DLB, compared by a non-parametric Mann–Whitney U-test. Graph displays mean ± SEM of the total PLA area in μm^2/image, with each dot representing one image. ****$p < 0.0001$. **e** Close-up z-stack rendering of a LB-containing neuron, with (left) and without (right) pS129, displaying the lack of PLA-staining of the LB. PLA-signal (red, arrows) and LB (grey, arrowhead) is highlighted. Smaller panels on the right show weak pS129 IF-labelling of PLA particles.

specific proximity probes play a major role in determining which α-synuclein species can be recognised by the PLA.

Having confirmed the functionality of the MJF-14 PLA using Navinci probes and kits in detecting signal in both neuropil and cell body compartments, we continued with setting up the expansion PLA with this kit.

We hypothesised that some of the neuropil PLA was likely located in the presynaptic terminal – the compartment where native α-synuclein primarily resides and a putative origin of α-synuclein aggregate pathology. Therefore, samples were labelled with fluorescent Navinci MJF-14 PLA, followed by immunostaining for excitatory presynapses (VGLUT1) and
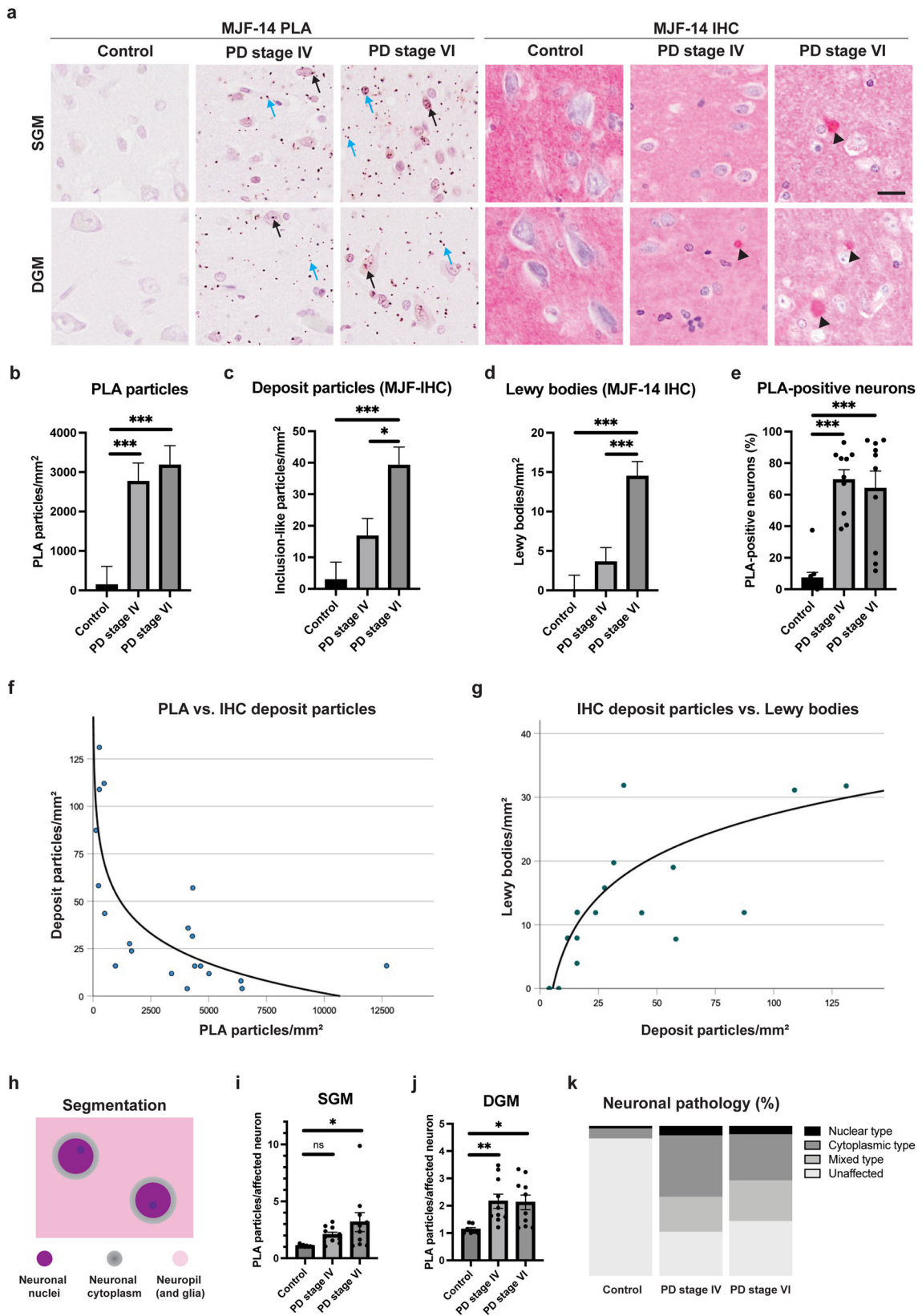
total α-synuclein using an α-synuclein-specific nanobody (Asyn-Nb)[75]. Confocal imaging of non-expanded samples confirmed staining protocol functionality and did indeed indicate the likely co-localisation of a fraction of the MJF-14 PLA signal with VGLUT1 in the DLB motor cortex (Supplementary Fig. 7, arrows). As for the chromogenic application, virtually no PLA signal was found in the control motor cortex (Supplementary Fig. 7).

Following the expansion procedure, gel pieces were excised and placed in a specially designed imaging chamber (see sketch in Fig. 5a), removing as

Fig. 4 | MJF-14 PLA efficiently distinguishes PD patients from controls but does not discriminate between stage IV and stage VI PD in the anterior cingulate cortex. a Representative images comparing MJF-14 PLA and MJF-14 IHC in the superficial (SGM) and deep (DGM) layers of the ACC from control, Braak stage IV, and Braak stage VI PD. Black arrows indicate neuronal PLA, blue arrows indicate glial and neuropil PLA signals, and arrowheads highlight deposit particles/LBs. Scale bar = 20 μm. **b** Quantification of the total PLA particle count per mm^2. The control group is significantly different from the two PD groups ($p < 0.001$). **c** Quantification of the total deposit particle count per mm^2 (detected by IHC). PD stage VI is significantly different from both controls ($p < 0.001$) and PD stage IV ($p = 0.011$). **d** Quantification of LB count per mm^2. PD stage VI is significantly different from both controls and PD stage IV ($p < 0.001$). Values plotted in (**b–d**) can be found in Suppl. Table 4. **e** Percentage of neurons containing PLA particles (averaged for SGM and DGM). Each subject is indicated as a dot. Both PD groups are significantly different from controls ($p < 0.001$), but not from each other ($p = 0.409$). For more information, see Suppl. Table 5. **f** Correlation between PLA particles and deposit particles (IHC) in PD stage VI. The density of PLA particles is inversely logarithmically correlated with the density of deposit particles (r_s [20] = −0.732, $p < 0.001$).

g Correlation between deposit particles and LBs in PD stage VI. The density of LBs is positively correlated with the density of deposit particles (r_s [20] = 0.675, $p = 0.001$). **h** Schematic representation of image segmentation for analysis: PLA pathology is analysed inside neuronal cell bodies (in nuclei (purple) and/or assumed cytoplasm (grey)) as well as away from neuronal cell bodies (denoted neuropil, but also containing glia (pink)). **i** Quantification of the average PLA particle count per affected neuron in SGM, with each subject indicated as one dot. There are significantly more PLA particles in affected neurons of PD stage VI than controls ($p = 0.011$) and a similar non-significant tendency for PD stage IV ($p = 0.218$). **j** Quantification of the average PLA particle count per affected neuron in DGM, with each subject indicated as one dot. The control group is significantly different from both PD stage IV ($p = 0.007$) and stage VI ($p = 0.011$). Values plotted in (**i, j**) can be found in Supplementary Table 6. **k** Proportion of different types of neuronal pathology, gradient grey coded for unaffected, solely nuclear, solely cytoplasmic, or mixed nuclear and cytoplasmic types. Values used for generating the graphic can be found in Supplementary Table 7. Data are displayed as mean ± SEM, averaged for SGM and DGM unless otherwise indicated, and comparisons are made using univariate analyses covarying with age, sex and post-mortem delay. *$p < 0.05$, **$p < 0.01$, ***$p < 0.001$.

Table 1 | Demography of the human anterior cingulate cortex cohort (data presented as mean ± SD)

	Control	PD stage IV	PD stage VI	P-value
Sex (M/F)	5/5	5/5	6/4	0.88 (χ^2)
Age (years)	78 ± 10	77 ± 6	80 ± 4	0.57 (ANOVA)
Post-mortem delay (hours)	15 ± 6	14 ± 8	9 ± 10	0.22 (ANOVA)
Disease duration (years)	-	13 ± 2	14 ± 8	0.32 (T)

much liquid from the gel as possible to allow stable STED imaging. From expanded samples, MJF-14 PLA signal was indeed found in small areas positive for VGLUT1, resembling the putative sizes of individual excitatory presynapses of 0.5–2 μm in diameter[76–79], demonstrating the presence of presynaptic α-synuclein aggregates (Fig. 5b, c). Examples of MJF-14 PLA signals not co-localising with VGLUT1 were also found, signifying aggregates present in other cellular compartments, different types of (VGLUT1-negative) presynapses, or other cell types (Fig. 5d, e). MJF-14 PLA signal, however, predominantly coincided with total α-synuclein nanobody staining (Fig. 5b–e), confirming the presence of α-synuclein at sites of PLA signal. The usage of the α-synuclein nanobody also facilitated the precise localisation of the α-synuclein in our samples, as linkage errors become a significant factor to account for after the expansion procedure. Since the expansion procedure isotropically expands everything in our samples, linkage error, i.e., the distance between fluorophores (which we observe) and actual targets (which we want to locate) is also expanded. The size of the linkage error thus depends on the combined size of our antibody/nanobody and fluorophore. As such, a linkage error of at least 20 nm is expected for VGLUT1 signals (stained with primary + secondary antibody, approx. 150 kDa each) and for the PLA, a linkage error around 50–60 nm is not unexpected[80]. In contrast, using tagged nanobodies (approx. 15–20 kDa in size) the typical linkage error is much lower, around 7–9 nm, allowing us to confidently localise the α-synuclein. Despite the limitations that the linkage errors pose in our experiments, the expansion PLA provides convincing documentation of α-synuclein aggregates in excitatory presynapses.

MJF-14 PLA is not specific to α-synuclein in mouse models

To assess the appearance and distribution of MJF-14 PLA in a mouse model of PD, we next compared signals in male human α-synuclein transgenic mice (Thy1-hasyn-Tg, line 61; ASO) and α-synuclein knockout (C57BL/6N-Sncatm1Mjff; ASKO) mice. Surprisingly, substantial amounts of MJF-14 signal were detected in both ASO and ASKO mice, with region-dependent

variations, i.e., highest signal in midbrain and lowest in hippocampus (Fig. 6a). Technical negative controls, omitting either the PLA probe-conjugated antibodies or the ligase in the PLA reaction showed essentially no signal (Supplementary Fig. 8a), demonstrating that the signal was not due to incomplete blocking of endogenous peroxidases. Moreover, the signal was present in ASKO mice through different batches of antibodies/PLA probes (data not shown). We also compared the results of the MJF-14-conjugated Duolink probes (Sigma) with MJF-14-conjugated Naveni PLA probes (Navinci), which yielded a similar PLA signal in ASKO mice (Fig. 6a, b). It was not possible to dilute the PLA probes so that no signal was present in ASKO without simultaneously losing all signals in the ASO mice (Supplementary Fig. 9).

To exclude the possibility that the presence of the signal was caused by an artefact with our ASKO mouse strain (ASKO #1; C57BL/6N-Sncatm1Mjff), we obtained a second ASKO mouse strain (ASKO strain #2; B6(Cg)-Sncatm1.2Vlb/J) for comparison. This second ASKO strain also stained positive for MJF-14 PLA, albeit with more signal in the cortex and hippocampal regions and less in the midbrain, demonstrating that MJF-14 PLA positivity in ASKO mice is consistent across strains (Fig. 6c). To examine whether the signal could be due to binding to another mouse synuclein isoform, we also included α-/β-/γ-synuclein triple knockout (TKO) and α-/β-synuclein double knockout (A/B-KO) mice in the analysis. The TKO mice were completely negative for MJF-14 PLA (Fig. 6c), indicating a cross-detection of either β- or γ-synuclein, most likely β-synuclein where the 5 C-terminal residues are identical to α-synuclein[81]. Indeed, MJF-14 PLA-staining of A/B-KO mice also didn't produce any signal, determining mouse β-synuclein as the culprit (Fig. 6d). MJF-14 immunohistochemistry on parallel sections also resulted in staining in both WT and ASKO strain #2 mice, while TKO and A/B-KO mice remained blank, confirming that the signal presence in ASKO mice is antibody-dependent (Supplementary Fig. 8b). Of note, the MJF-14 antibody has been used successfully for detection of α-synuclein aggregate pathology by IHC/IF in mouse models, made possible by the dense epitope presentation in larger aggregates/inclusions compared to the more diffuse non-specific staining[64,82–84]. The PLA technique, in contrast, allows amplification of low-abundance signals—provided that the complementary probes are present in the required proximity—but offers no difference in signal intensity to distinguish specific from non-specific signal. Thus, we concluded that the MJF-14 antibody is not suitable for PLA in mouse models due to the strong background staining in ASKO mice, which could not be separated from potentially true α-synuclein PLA staining in transgenic mice.

Discussion

In this study, we present an α-synuclein PLA based on the aggregate-selective MJF-14 antibody and evaluate its functionality in synucleinopathy
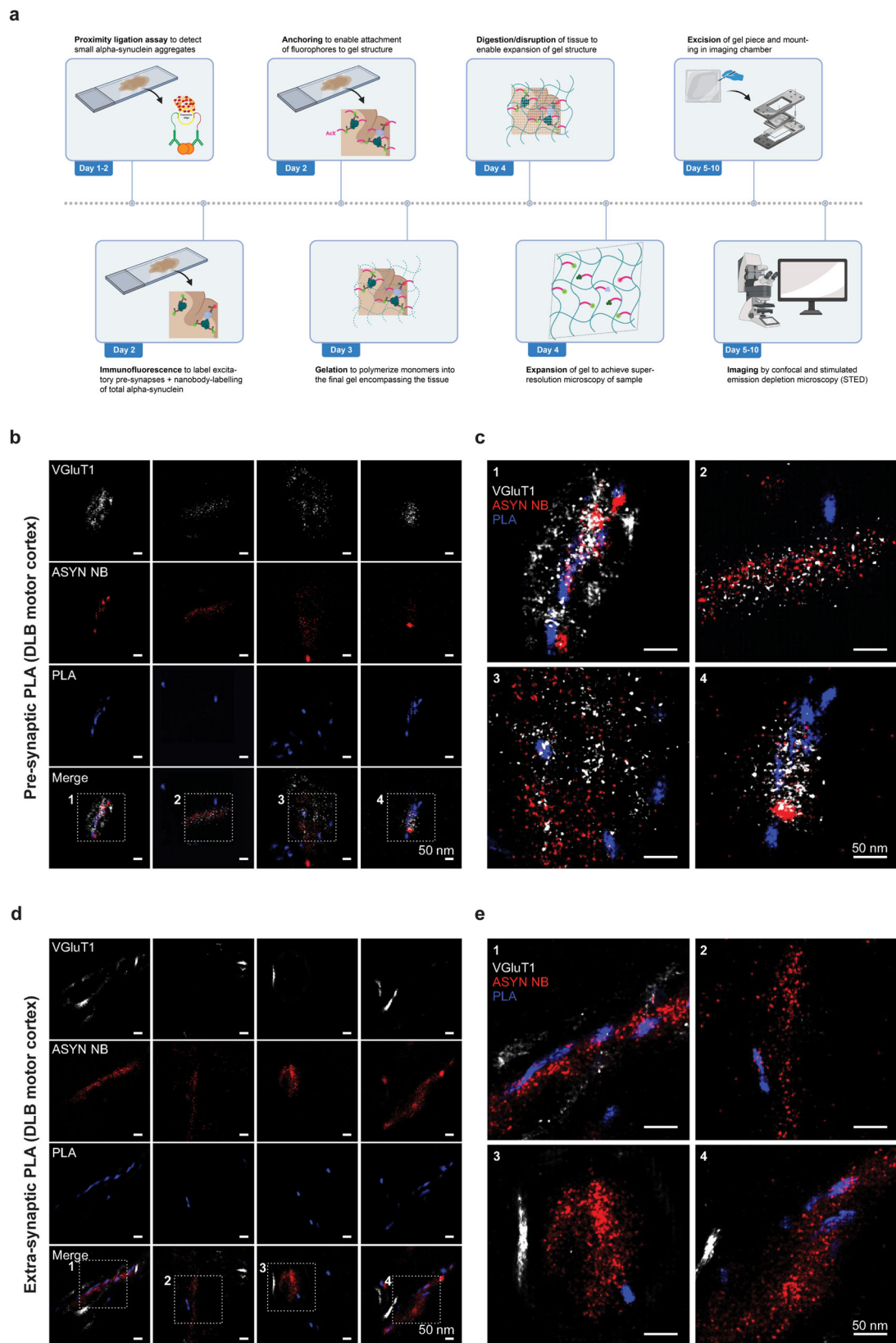
Fig. 5 | Applying ONE microscopy to PLA imaging decisively identifies α-synuclein aggregates at the presynaptic terminal in DLB motor cortex.
a Experimental setup of ONE microscopy combined with MJF-14 PLA. Samples were stained for MJF-14 PLA, then VGLUT1 and total α-synuclein, before tissue expansion and ONE imaging of gels. **b–e** Individual channel + merged images from DLB motor cortex. VGLUT1 (white) labels excitatory presynapses, MJF-14 PLA (blue) labels small α-synuclein aggregates, and Asyn-Nb (red) labels total α-synuclein. **b**, **c** Examples of presynaptic PLA shown by co-localisation of PLA signal with both total α-synuclein and VGLUT1. **d**, **e** Examples of extra-synaptic PLA, identified by co-localisation of PLA signal with total α-synuclein but not with VGLUT1. All scale bars = 50 nm. Panel (**a**) is created with BioRender.com.
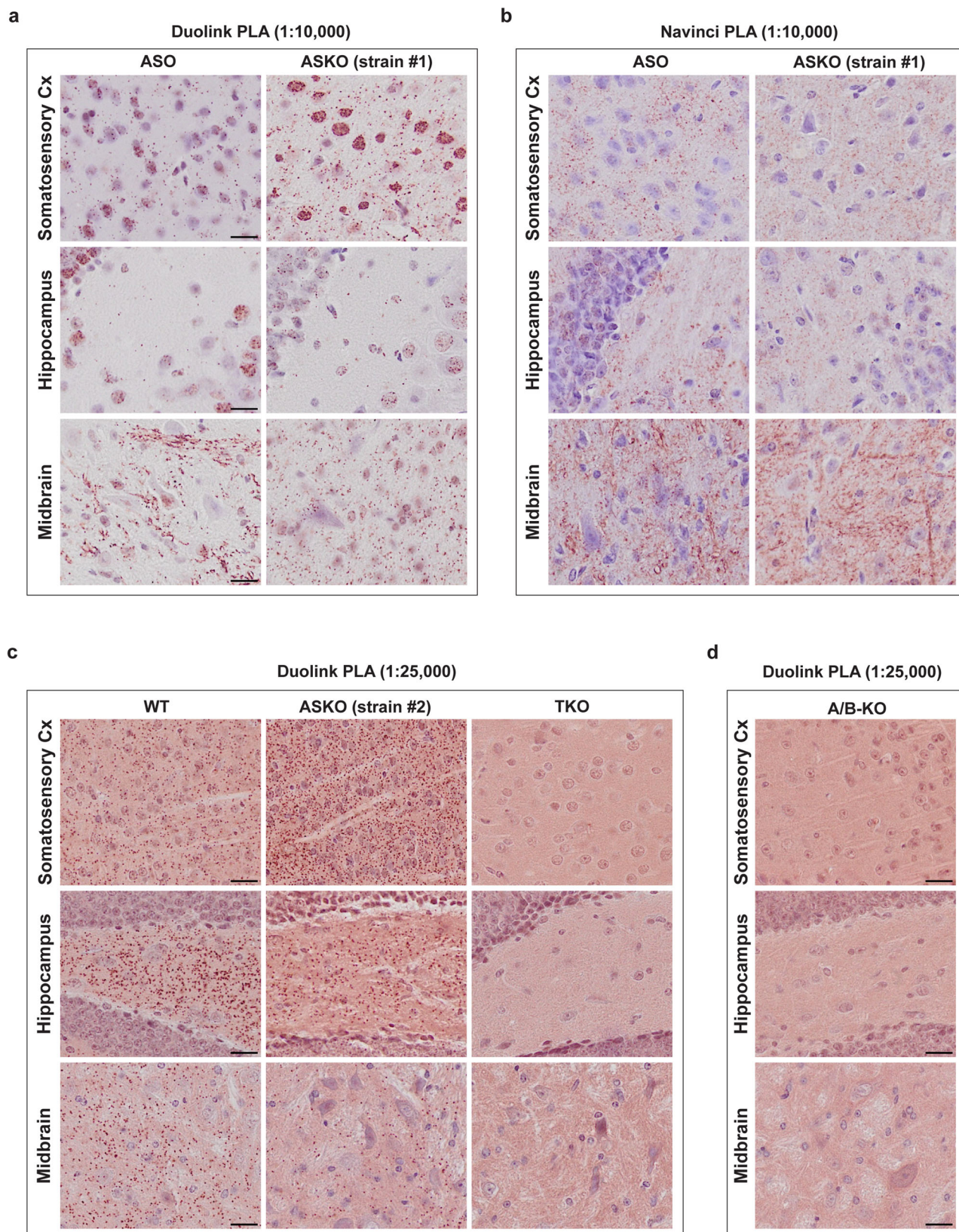
Fig. 6 | MJF-14 PLA signal is not specific for α-synuclein in mouse models.
a Comparison of MJF-14 PLA signal in α-synuclein transgenic (ASO) and α-synuclein knockout (ASKO strain #1) mice, using PLA probes and detection kits from Duolink (Sigma). **b** Similar comparison of MJF-14 PLA signal as in (**a**) but using PLA probes and detection kits from Navinci. **c** MJF-14 PLA signal in a different α-synuclein knockout strain (ASKO strain #2), compared with WT, and triple α-/β-/γ-synuclein knockout mice (TKO). **d** MJF-14 PLA signal in α-/β-synuclein double knockout mice (A/B-KO). All scale bars = 20 μm.

Article

models as well as post-mortem patient tissue. We show that aggregation is a prerequisite for MJF-14 PLA signal formation, based on the significant decrease in signal in our cell model upon treatment with aggregation inhibitor ASI1D. No similar decrease in syn211 PLA signal was seen following ASI1D-treatment, despite the fact that Roberts et al. also showed a need for multimerization, based on bimolecular fluorescence complementation, in order to generate syn211 PLA signal[46]. The differences between the MJF-14 and the syn211 PLAs observed in this study may be caused by the syn211 PLA targeting multimers—including potential physiological polymers[55–58]. As highlighted by Estaun-Panzano et al., the PLA technique in itself does not provide any selectivity towards pathological aggregates[85], but the preference of the MJF-14 antibody for pathological aggregates may confer such quality. Though some detection of monomers by the MJF-14 antibody has been shown (particularly if samples are denatured), multiple studies have demonstrated a strong preference of the antibody for aggregated (oligomeric and fibrillar) species[42,47,48]. Indeed, surface plasmon resonance analysis by Kumar et al. showed that MJF-14 binds with more than 4300x higher affinity to oligomeric α-synuclein than monomeric[42].

The utility of the MJF-14 antibody, in both PLA and IF applications, is further underscored by its potential in models combining it with MJF-14-invisible AS-141G PFFs to induce α-synuclein pathology. This allows a confident examination of endogenous α-synuclein aggregation without the risk of cross-detection of the added PFFs. As the AS-141G PFFs were also engineered to be S129A-mutated, and thereby non-phosphorylatable at serine-129, pS129-α-synuclein-specific antibodies will also only stain endogenous α-synuclein in this setup[60]. Thereby, these tools enable detailed studies into the early aggregation and phosphorylation processes and can be combined with a range of model systems.

The clinical material studied in this paper consisted of a PD/control cohort from anterior cingulate cortex ($n = 10$ per group) and a DLB/control cohort from the superior frontal cortex and motor cortex ($n = 2$ per group). The PD cohort was used to compare MJF-14 PLA directly with IHC and study the distinction in pathology at stage IV vs. VI PD, while the DLB cohort was used to study the LB-labelling capacity of the MJF-14 PLA and compare its detection ability between different company kits (Duolink vs. Navinci MJF-14 PLA). Especially the PD cohort, with 10 stage IV and 10 stage VI PD patients, is larger and more homogeneous than what has previously been published in PLA studies of α-synuclein pathology and brings forth new clinical insight as discussed below. In both the PD and DLB cohorts, we found striking amounts of MJF-14 PLA signal, indicating a much more widespread dysfunction in these tissues than what is revealed using IHC staining with either pS129- or conformation-specific α-synuclein antibodies. Furthermore, the comparison of stage IV and VI PD implied the ability of the MJF-14 PLA to detect pathology that markedly precedes bona fide inclusions in human brains as the Braak stage IV cases were essentially devoid of LBs in the ACC. Thereby, our data support the findings from Sekiya et al., who reported oligomeric pathology using the syn211 PLA in multiple hippocampal and cortical regions of stage III–IV PD without concurrent presence of Lewy-related pathology[54]. Although they did not examine the ACC, a previous paper from the same group demonstrated PLA-positivity in 4/5 PD patients in the ACC, in the form of "punctate" staining[52]. While difficult to directly compare results between studies, all PD cases in our cohort were PLA-positive in the ACC. This difference could be explained by a higher sensitivity of the MJF-14 PLA or by the detection of different aggregates/polymers by the two PLAs, as mentioned above. Alternatively, the use of distinct Braak stages could influence the findings, as Sekiya et al. included 5 cases of stage III–VI, of which one stage III case was void of PLA signal in the ACC[52], while we examined 10 stage IV and 10 stage VI cases.

In the PD cohort, we found considerable variability in the density of PLA pathology between cases in the PD groups—a characteristic that was independent of their Braak stage. Half of the patients in both stage IV and VI in our cohort displayed PLA pathology in more than 80% of the neurons detected by automated analysis, suggesting an extensive neuronal

dysfunction in this area. Conversely, in stage VI, there were 3/10 patients in which fewer than 25% of the neurons (range 11.7—22.9%) contained PLA pathology (see Fig. 4e). This suggests that the Braak staging is likely not sufficient for properly characterising the molecular α-synuclein pathology in PD patients, as has previously been indicated[21,86–88]. Instead, standard staging schemes should be complemented by other methods to increase our understanding of disease including examination of various post-translational modifications, for example[89]. Whether this inter-individual variation seen in the two PD groups might be caused by different subtypes of PD, for instance brain-first and body-first as recently suggested by Borghammer and colleagues[90–93], or related to, e.g., genetic autophagy-lysosomal-related risk factors of sporadic PD, can at present only be speculated upon. Nevertheless, this degree of variability between patients of the same Braak stage exposed by proximity ligation has not previously been reported—perhaps because earlier studies have only used smaller groups of mixed disease stages[46,52,54].

To characterise the α-synuclein pathology in the PD cohort, we employed three different measures: PLA particles, deposit particles (i.e., any accumulation of aggregated α-synuclein with a minimum length of 2 µm), and LBs (manually counted round or oval-shaped inclusions of minimum 5 µm), the latter two based on MJF-14 IHC. The use of both the strict LB count and the broader deposit particle definition allowed us to confidently demonstrate that the PLA does indeed detect different and earlier α-synuclein depositions. From this, we discovered an inverse correlation between PLA particle density and the density of α-synuclein deposit particles (detected by IHC) in the stage VI PD patients. Combined with the observation that LB-containing neurons in DLB harbour less PLA signal than neighbouring LB-negative neurons, this indicates that α-synuclein inclusions may be able to sequester PLA-positive aggregates and convert them into (Duolink MJF-14) PLA-negative species. As multiple studies have shown that the classical Lewy pathology is not a good measure for estimating either neuronal death or symptomatic burden of patients[21,22,94], our results raise the speculation whether the PLA pathology might correlate better with impact on cellular functions or disease progression. Additionally, our results further weigh into the discussion of whether the LB is in itself a toxic species, a – perhaps failing—protective response that sequesters potentially toxic species, or simply a bystander in synucleinopathies[11,19,20,22,23,94,95].

In several of the experiments presented in this paper, we detected PLA particles apparently located in the nuclei, both in cell models and in post-mortem human brain. Curiously, in the human brain, it appeared that the chromogenic PLA setup detected more nuclear PLA signal, as well as more neuropil PLA signal, than the fluorescent PLA setup did. This distinction might be methodology-related, perhaps due to a higher sensitivity of the chromogenic setup when compared to the fluorescent PLA after the auto-fluorescence quenching. As the fluorescent PLA setup did show nuclear PLA detection in the cell models employed here, it is clearly not a general deficiency in the fluorescent PLA setup. Alternatively, it is possible that the fluorescent PLA images from the DLB cases presented in Fig. 3 simply originate from a (sub)region in the brain with very little nuclear and more cytoplasmic PLA compared to, e.g., the ACC.

Though the presence of nuclear α-synuclein has been disregarded and sometimes considered an artefact caused by cross-reactivity of pS129-α-synuclein antibodies[96,97], nuclear α-synuclein inclusions are well-characterised in MSA[98–100]. In recent years, putative physiological roles for the nuclear presence of α-synuclein have started to emerge, including DNA binding and modulation of DNA repair[101]. Additionally, several studies have shown molecular changes, including transcriptional dysregulation and altered ribosomal RNA processing, following overexpression of α-synuclein in the nuclei[102–105]. These deficits have been suggested to cause specific symptoms such as anxiety and cognitive impairment as well as cellular toxicity[100,103,105,106]. Combined with the recent demonstration of oligomeric α-synuclein within the nuclei in DLB brains by Koss et al.[107], these studies support the relevance of the nuclear MJF-14 PLA signal detected in this study. While we did not assess potential correlations between nuclear (or total) PLA and clinical symptoms in our cohorts, Sekiya et al. showed that

cognitive impairment in their PD cohort correlated with syn211 α-synuclein PLA signal in the hippocampus[54]. Though their correlation was based on a semi-quantitative assessment of PLA signal density and did not account for specific distribution of PLA signal within nuclei or not, no similar correlation was seen between cognitive impairment and Lewy-related pathology. Thus, these results highlight the potential of PLAs in providing a link between clinical symptoms and neuropathology.

A curious observation in this study was that not only the selected antibody but also the specific brand of PLA kit plays a crucial role in determining which α-synuclein species are detected in the PLA. As such, the Duolink MJF-14 PLA did not show efficient labelling of LBs in either DLB frontal and motor cortex or in PD anterior cingulate cortex. In contrast, the Navinci MJF-14 PLA, although only tested on the DLB motor cortex, displayed a strong labelling of LBs in addition to the labelling of non-inclusion aggregate pathology. As the specific kit formulations, including the structure of PLA probes, are proprietary to both Duolink and Navinci, we can only conclude that careful validation is necessary when switching between kit suppliers. Adding to the complexity, although Roberts et al. also showed an overall predilection of the syn211 PLA towards non-LB pathology, their assay showed a stronger detection of cortical LBs than with regular immunohistochemistry in both PD and DLB patients[46]. Collectively, we are left with two versions of the new MJF-14 PLA: a version with a high specificity towards early α-synuclein pathology and only sparse labelling of inclusions (Duolink), and another version that appears to label all α-synuclein pathology, whether organised into inclusions or not (Navinci). The discrepancy between the detected species with the two PLA kits is likely caused by distinct oligonucleotide linker composition, which could allow for more or less flexibility in epitope binding and subsequent linker ligation. For some applications, such as pathological examinations, the Navinci MJF-14 PLA could be ideal in that it would allow the examination of a wider spectrum of α-synuclein pathology in one slide. This would of course need validation to elucidate whether this PLA does indeed recognise LBs and other α-synuclein inclusions as efficiently as the current standard IHC methods. On the other hand, one could also imagine applications where a preference for non-inclusion α-synuclein pathology is more suitable, in which case the Duolink MJF-14 PLA would be superior. At the structural level, the different specificity of the two kits suggests that modifying the oligonucleotide linkers, which are conjugated to the MJF-14 antibody, holds promise for development of aggregate- or even strain-specific PLA reagents.

In this study, we present an assortment of analyses on PLA-stained samples, going beyond the scope of semi-quantitative measures based on scoring plates. These ranged from simple quantifications of PLA particle counts normalised to either cell number, field of view, or tissue area to more advanced quantifications of, e.g., PLA in various neuronal compartments or PLA in neurons with/without LBs. An interesting observation, based on the fluorescent MJF-14 PLA on both human cortical neurons and neuroblastoma cells, was that not only PLA particle count but also intensity varied across conditions. This phenomenon is most likely caused by the presence of multiple rolling circle amplification products on the same aggregate, indicating that the PLA-positive aggregates detected may also differ in size between conditions. It opens for considering PLA signal as not simply a dot or particle of inconsequential intensity, but something where analysis of integrated density (PLA area times intensity) may give further insight into aggregate dynamics. While several protocols for PLA analysis have been published, none has suggested integrated density as a measure of PLA signal, perhaps because PLAs are mostly applied to study protein interactions rather than aggregate dynamics[108–111].

Though this study presents the largest PD cohort so far studied with an α-synuclein PLA, it was limited to studying a single brain region from these cases. Likewise, the DLB cohort only contained two cases and two controls, leaving the conclusions from this cohort to be validated in larger studies. Nevertheless, our main purpose was to highlight the potential of PLA in synucleinopathy research, particularly combined with other methods (such as super-resolution microscopy) and analyses (including more quantitative single-neuron approaches) than previously presented.

For instance, by combining our PLA with expansion and STED microscopy, we demonstrated the presence of PLA-positive aggregates in excitatory presynapses in DLB motor cortex. Here, further studies to follow up on the other cellular compartments containing PLA signal as well as their quantitative distribution during the course of disease could be of great value. Additional studies of multiple brain regions for their PLA-detected α-synuclein pathology are also warranted, especially regions previously considered negative for pathology, such as the cerebellum in PD, where PLA signal has already been demonstrated in a few cases[52]. Though the α-synuclein PLAs have proven a strong tool for detection of earlier types of aggregate pathology than the LBs, an exact characterisation of the detected α-synuclein species is still lacking. Such a characterisation should be based on patient-derived α-synuclein species rather than in vitro-generated oligomers and fibrils, as the in vitro-generated species may not reflect the range and complexity of the species found in patients[112,113].

Other limitations of this study concern the segmentation of signals in the PD cohort, in particular the definition of neuronal nuclei and their respective cytoplasm. Since the sections included in the study were only counterstained with the nuclear dye haematoxylin, neuronal nuclei were distinguished from glial nuclei solely based on differences in size, which does not allow a clear-cut distinction. Similarly, cytoplasm was only rarely stained by the counterstain and, consequently, in the analysis the cytoplasm was estimated as a circular border around the nucleus, based on average measurements of cytoplasm within neurons with visible cytoplasm. These limitations could be overcome by the use of other counterstaining methods, or co-staining with specific neuronal or other cell type markers in future. In the automation process, we were additionally challenged by variations in the counterstaining efficiency, which left some of the sections rather faintly counterstained, despite being stained in the same batch as other sections with much brighter counterstain. In the end, we had to divide sections into two groups depending on counterstain efficiency and develop distinct classifiers for these groups. Although not optimal, it was not possible to achieve anything close to a satisfactory segmentation using only one classifier, while using two classifiers, we achieved a sensitivity for recognition of neuronal nuclei of 85% (Supplementary Fig. 3). Also, as there was no significant difference between controls and the two PD groups in counterstain efficiency ($p = 0.37$), we were assured that the classifiers did not accidentally skew the analysis.

Lastly, we discovered that the MJF-14 PLA was not functional in mouse models due to a cross-detection of β-synuclein and a resulting large background signal, even in α-synuclein knockout mice. This cross-detection did not appear to be an issue for human tissue, as demonstrated by the blank regions of interest in control ACC (Fig. 4). Nevertheless, this means that there are currently no published options for α-synuclein PLA on mouse models only expressing mouse α-synuclein, as the syn211 antibody is human-specific and therefore cannot recognise aggregates of mouse α-synuclein. Development of an α-synuclein PLA functional in mouse models regardless of their expression of mouse and/or human α-synuclein would be of great value, both in terms of basic understanding of aggregate pathology and for the evaluation of pre-clinical treatments targeting α-synuclein aggregation.

In conclusion, we here demonstrate an α-synuclein PLA with increased specificity towards early-stage α-synuclein aggregate pathology. We highlight combinations of PLA with super-resolution imaging techniques and with specialised AS-141G PFFs, which are invisible to the MJF-14 antibody in both PLA and IF applications. We underscore the fact that α-synuclein pathology detected by MJF-14 PLA in PD is much more widespread than and precedes Lewy pathology detected by IHC, with on average 67% of the neurons affected by PLA pathology in the cingulate cortex of both stage IV and VI PD patients. In comparison, only 4% of neurons contained LBs even in stage VI patients. Finally, we provide a method for extensive automated analysis of chromogenic PLA-stained tissue sections, thereby setting the scene for comprehensive large-scale clinical studies of non-inclusion α-synuclein aggregate pathology, which has not hitherto been appreciated.

Methods

Protein production, purification and fibril assembly

Full-length S129A-mutated human α-synuclein and S129A-mutated human α-synuclein with an added glycine residue at the C-terminal (S129A-α-synuclein-141G) was expressed in BL21(DE3)-competent cells and purified by reverse phase chromatography as previously described[60,114,115]. PFFs of the two types of α-synuclein were prepared in parallel by incubating the soluble monomeric α-synuclein (4 mg/mL) in PBS at 37 °C with 1050 rpm shaking for 72 h, before collection, characterisation, and storage as previously described[60,82,116]. Immediately before use, aliquots of PFFs were quickly thawed and sonicated briefly using a Branson SFX 250 sonifer (0.3 s on, 0.7 s off, 30% power, for 45 pulses). Sonicated aliquots were stored at room temperature until use.

Cell culture

Human neuroblastoma (SH-SY5Y) cells with inducible expression of α-synuclein[49] were grown in Roswell Park Memorial Institute (RPMI) 1640 medium (Lonza, #BE12-702F) supplemented with 15% foetal bovine serum (Biowest, #S1810), 50 units/mL penicillin and 50 μg/mL streptomycin (Merck, #A2213), 200 μg/mL geneticin (G418, TCI EUROPE, #TCIAG0349), 50 μg/mL hygromycin B (Gibco, #10687010), and 1 μg/mL doxycycline (Calbiochem, #324385). On day 0, cells were seeded onto coverslips and α-synuclein expression was induced in some cultures by the removal of doxycycline. For all experiments, mitotic SH-SY5Y cells were differentiated into non-mitotic neuronal cells by the addition of 20 μM all-trans retinoic acid on day 1 (Molecular Probes/Invitrogen, #207340010). From day 1 onwards, 20 μM of ASI1D was added to inhibit aggregation of α-synuclein in some of the cultures (>98% pure H-RGGAVVTGRRRRRR-NH$_2$ (Schafer-N), 10 mM stock in 98% ethanol)[51]. At 7 days post expression of α-synuclein, cells were fixed in 4% PFA.

Human cortical neurons

Human embryonic stem cells (hESCs) NN3053 (Novo Nordisk) were differentiated to cortical neurons in a similar manner to what has been previously described[117,118]. Briefly, NN3053 hESCs were plated on Laminin-521 in mTeSR1 medium with 10 μM Rock inhibitor Y-27632 (Tocris Bioscience). The following day, media was changed to CPN medium (1:1 DMEM/F12 and Neurobasal with 0.5x B27, 0.5x N2, 0.5x ITSA, 1x GlutaMAX, 0.5x penicillin/streptomycin, and 50 μM 2-mercaptoethanol (Life Technologies)) and supplemented with 100 nM LDN193189 (Stemgent) and 10 mM SB431542 (Tocris Bioscience). Media was changed every second day or as required. On day 11 neural progenitors were passaged with gentle dissociation buffer (PBS supplemented with 0.5 mM EDTA) and reseeded on laminin-521 coated plates at a split ratio of 1:2.5 in CPN medium supplemented with 20 ng/mL fibroblast growth factor 2 (FGF2; R&D Systems) and 10 μM Y-27632. The following day, media were changed to CPN basal media containing 20 ng/mL FGF2. On day 18 cells were passaged with gentle dissociation buffer and reseeded at 60,000 cells/cm^2 on laminin-521 in CPN medium supplemented with 10 μM Y-27632. The following day media was changed to CPN medium and from then changed as required. On day 25, cells were plated on Laminin-521 coated plates at 90,000 cells/cm^2 in CPN basal media supplemented with 10 μM Y-27632, 200 nM ascorbic acid (AA; Sigma-Aldrich), 0.05 mM dcAMP (Sigma-Aldrich), 40 ng/mL GDNF (R&D systems). The following day and onwards, media was changed to Pan-neuronal medium (1:1 DMEM/F12 and Neurobasal with 0.5x B27, 0.5x N2, 1x GlutaMAX, 0.5x penicillin/streptomycin, and 1x NEAA (Life Technologies)) supplemented with 200 nM AA, 0.05 mM dcAMP, 40 ng/mL GDNF, 2 μM LM22A4 (Tocris Bioscience), 2.5 μM DAPT (Tocris Bioscience), and 1 ug/mL laminin (Sigma-Aldrich).

On day 35, Pan-neuronal medium with supplements was prepared with 42 μg/mL of either S129A or S129A-α-synuclein-141G (AS-141G) PFFs, or a similar volume of sterile PBS. One third of the medium was replaced in each well, resulting in a final concentration of PFFs of 14 μg/mL.

Neurons were fixed at either 2 h or 7 days post treatment, with the regular media change schedule resumed after 24 h of treatment. After fixation in 4% PFA, cultures were dried completely to increase adhesion to glass slides, before addition of PBS and storage at 4 °C until staining. Cultures were subjected to either a combined PLA and immunofluorescence (IF) protocol or to IF only.

Animal tissue

All procedures involving animals were conducted in accordance with the European directive on animal experiments (2010/63/EU), and the studies were approved by the Danish Animal Experiments Inspectorate (license no. 2017-15-0201-01203). All mice were housed in a temperature-controlled room under 12 h light/dark cycles with unlimited access to food and water.

To study the usability of MJF-14 PLA in mouse models, we employed a range of different mouse strains. These included wild-type C57Bl6 mice (WT), α-synuclein transgenic mice (line 61; B6;DBA-Tg(Thy1-SNCA) 61Ema[119]) overexpressing human α-synuclein (ASO, males only), two different strains of α-synuclein knockout mice (ASKO #1; SNCA$^{-/-}$; C57BL/6N-Sncatm1Mjff/J; JAX stock #016123[120], and ASKO #2; SNCA$^{-/-}$; B6(Cg)-Sncatm1.2Vlb/J; JAX stock #028559[121,122]), α-/β-synuclein double knockout mice (A/B-KO) and α-/β-/γ-synuclein triple knockout mice (TKO). A/B-KO and TKO mice were generated as described by Connor-Robson et al., albeit using the ASKO strain #2 for α-synuclein knockout[123]. All mice studied were adult (~4–13 months old) and we studied 2–4 mice of each strain. The total number of experimental mice used in this study was 17.

Mice were sacrificed by intraperitoneal injection of lethal dosage of pentobarbital and perfused with PBS followed by 4% PFA, both containing phosphatase inhibitors (25 mM β-glycerolphosphate, 5 mM NaF, 1 mM Na$_3$VO$_4$, and 10 mM Na-pyrophosphate) before removing the brain. Brains were post-fixed in 4% PFA for 24 h and then stored in PBS with 0.05% sodium azide before paraffin-embedding and microtome sectioning at 8–10 μm.

Human tissue

Human post-mortem brain tissue was obtained from New South Wales Tissue Resource Centre at the University of Sydney and the Sydney Brain Bank at Neuroscience Research Australia. The study was approved by the University of Sydney Human Research Ethics Committee (2017/985).

As we have shown previously the anterior cingulate cortex (ACC) has staged α-synuclein changes in PD with increased levels but limited LBs at stage IV progressing to significant LBs by stage VI[67], we requested formalin-fixed paraffin-embedded (FFPE) tissue sections from the ACC for this study. Brain samples from pathologically confirmed subjects with PD ($n = 10$ Braak stage IV; $n = 10$ Braak stage VI) and controls without any neurological or neuropathological disease ($n = 10$) were obtained (see Table 1). Controls were matched for age (average 77–80 y) and post-mortem delay (average 9–15 h). All cases with PD were levodopa-responsive and met the UK Brain Bank Clinical Criteria for a diagnosis of PD with no other neurodegenerative conditions. PD and control cases were assessed according to the regional presence of Lewy pathology as defined by Braak et al.[17], with all controls having no Lewy pathology and the PD cases having Braak stage IV or VI Lewy pathology. The mean disease duration did not differ between the stage IV (average 13 ± 2 y) and stage VI (average 14 ± 8 y) groups (see Table 1).

To assess the ability of the PLA to detect LBs and assess neuropil PLA localisation, FFPE sections from the superior frontal cortex and motor cortex of patients with DLB ($n = 2$) and from non-neurodegenerative controls ($n = 2$) were similarly obtained from the Sydney Brain Bank. Average age was 82 years (range 80–84 y) and post-mortem delay in the range 9.5–14.5 h. Both DLB cases were Braak Lewy stage 6, with Braak tangle stage 0–1 and mild-moderate CERAD neuritic plaques, while the controls had no Lewy or significant age-related pathologies. Demographics of the DLB cases are summarised in Suppl. Table 1.

FFPE sections were cut on a rotary microtome (Thermo/Microm, #HM325) at 8 μm and mounted on Series 2 adhesive slides (Trajan Scientific Medical).

Table 2 | Parameters for proximity ligation assay in various models

Cell or tissue	Staining method[a]	Permeabilization, peroxide quenching and blocking times	Primary antibody dilution	Ligation time	Amplification time
SH-SY5Y cells	Fluorescent MJF-14 PLA	30 min	1:10,000	1 h	3 h
	Fluorescent syn211 PLA	30 min (permeabilization) 1 h (blocking)	1:100	1 h	3 h
Human cortical neurons	Fluorescent MJF-14 PLA	30 min	1:10,000	1 h	3 h
Human DLB and control FFPE	Fluorescent MJF-14 PLA	1 h	1:50,000	1.5 h	3.5 h
Human PD and control ACC FFPE	Chromogenic MJF-14 PLA	1 h	1:1000	1.5 h	3 h
Human DLB and control FFPE (expansion PLA)	Fluorescent MJF-14 PLA (Navinci)	30 min (permeabilization) 1 h (blocking)	1:5000	30 min	60 min
Mouse FFPE	Chromogenic MJF-14 PLA (Duolink)	1 h	1:10,000/ 1:25,000	30 min	100 min
	Chromogenic MJF-14 PLA (Navinci)	1 h	1:10,000	30 min	60 min

[a]Unless otherwise specified, Duolink kits were used for the application.

Antibody conjugation for proximity ligation assay

PLA was carried out using either the Duolink PLA kits for brightfield (Sigma, #DUO92012) or fluorescent applications (Sigma, #DUO92008), NaveniBright HRP (Navinci, #NB.MR.HRP.100) for brightfield applications, or a custom-made detection kit utilising biotin in the fluorophore labelling process (similarly obtained from Navinci). Assays were performed using the conformation-specific α-synuclein antibody MJF-14 (MJFR-14-6-4-2; Abcam, #ab214033) or the total α-synuclein antibody syn211 (Abcam, #ab206675). MJF-14 is an aggregate-selective antibody, which recognises an epitope primarily present in aggregated forms of α-synuclein, as previously characterised[42,47,48].

For Duolink PLA applications, antibodies were conjugated to plus- and minus-oligonucleotides using the Duolink PLA Probemaker kits (Sigma, #DUO92009 and #DUO92010) according to manufacturer's protocol. In brief, 20 μL antibody was mixed with 2 μL conjugation buffer, added to the lyophilised oligonucleotides (plus- or minus-) and incubated overnight at room temperature (RT). 2 μL stop reagent was then added and incubated for 30 min at RT. Finally, 24 μL of storage solution was added and conjugated antibodies stored at 4 °C.

For Navinci PLA applications, MJF-14 was conjugated to Navenibody 1 and 2 oligonucleotides using the NaveniLink conjugation kit (Navinci, #NL.050) according to manufacturer's protocol. In brief, 10 μL of Modifier was added to 100 μL antibody, before mixing with the lyophilised oligonucleotides (Navenibody 1 or Navenibody 2) and incubated overnight at room temperature (RT). 10 μL of Quencher N was then added and incubated for 15 min at RT, and conjugated antibodies were stored at 4 °C.

In general, Duolink PLA probes and kits were used in this manuscript, except where specifically stated that Navinci PLA probes and kits were used instead.

Proximity ligation assay

The following general protocol was used to perform PLA, with slight variations in incubation times and antibody dilutions depending on cells/tissues and whether fluorescent or chromogenic PLA was performed. Exact incubation times and antibody dilutions can be found in Table 2. Unless otherwise mentioned, washing was performed in 1x TBS + 0.05% Tween-20, except for TrueBlack-quenched sections, which were only washed in 1x PBS (detergent-free). For paraffin sections, initial deparaffinization and rehydration steps were followed by heat-induced epitope retrieval in 1x citrate buffer at pH 6.1 (DAKO, #S1699). All samples were then permeabilized in 0.5% Triton X-100 in PBS, followed by endogenous peroxide quenching in 0.3% hydrogen peroxide (for chromogenic PLA) or autofluorescence quenching with 1x TrueBlack (Biotium, #23007) in 70% ethanol (for fluorescent PLA on post-mortem human brain). Samples were

then blocked in 10% bovine serum albumin (BSA; Duolink MJF-14 PLA), 1x Duolink Blocking Solution (syn211 PLA), or 1x Naveni Blocking Buffer with Supplement 1 (Navinci MJF-14 PLA). For Duolink protocols, conjugated primary antibodies were diluted in 5% BSA (MJF-14 PLA) or in 1x Duolink Probe Diluent (syn211 PLA) and incubated for 1 h at 37 °C, followed by overnight incubation at 4 °C. For Navinci MJF-14 PLA, conjugated primary antibodies were diluted in 1x Primary Antibody Diluent with Supplement 2 and incubated overnight at 4 °C. Unbound antibody was washed off, and samples were incubated with Duolink ligation solution or Navinci Reaction 1 solution at 37 °C, followed by washing and subsequent incubation in Duolink amplification solution or Navinci Reaction 2 solution at 37 °C.

For fluorescent PLA, the amplification process was followed by washing, another round of blocking in 10% BSA and regular immunostaining with either rat α-tubulin (Abcam, #ab6160, 1:1000) or mouse pS129 α-synuclein (11A5, kindly provided by Imago Pharmaceuticals, 1:25,000) and chicken neuronal βIII-tubulin (TUJ1, LS Bio, #LS-B5225, 1:500) in 5% BSA, overnight at 4 °C. After washing off unbound antibody, samples were incubated for 1.5-3 hours at RT in secondary antibody (anti-rat AlexaFluor-488, #A21208, or anti-mouse AlexaFluor-488, Invitrogen #A11001, and anti-chicken AlexaFluor-647, Abcam #ab150175, as matching the primary antibodies) diluted 1:1000-1:2000 along with DAPI (4',6-diamidino-2-phenylindole, TH.GEYER, 5 μg/mL) in 5% BSA, again followed by washing. Then, samples were mounted with DAKO fluorescent mounting medium (DAKO, #S3023) and edges sealed with nail polish.

For chromogenic Duolink PLA, the amplification process was followed by washing and incubation in Duolink detection solution for 1 h at RT. After another round of washing, samples were incubated with Duolink substrate solution for 20 min at RT, washed again and nuclei counterstained with Duolink nuclear stain for 2 min at RT. Samples were left under running tap water for 10 min and then dehydrated in increasing concentrations of ethanol, incubated in NeoClear (Sigma, #109843), and mounted with DPX mounting medium (Sigma, #06522).

For chromogenic Navinci PLA, Reaction 2 was followed by washing twice in 1x TBS, then once in 0.1x TBS, and incubation in Navinci HRP reaction for 30 min at RT. After another round of washing in 1x TBS, samples were incubated with Navinci substrate reaction for 5 min, washed in dH$_2$O and nuclei counterstained with Navinci nuclear stain for 5 s. Samples were left under running tap water for 10 min and then quickly dehydrated in 100% isopropanol and mounted with VectaMount Express Mounting Medium (Vector Laboratories, #H-5700).

In all experiments, technical negative controls (either PLA without primary conjugated antibodies or PLA without ligase in the ligation reaction) were included to confirm the specificity of the observed signal. For

experiments on transgenic mice, we additionally employed biological negative controls in the form of α-synuclein knockout mice (ASKO, 2 strains), α-/β-synuclein double knockout mice, and α-/β-/γ-synuclein triple knockout mice.

Immunofluorescence (IF)

For IF of cultured human cortical neurons, all steps were performed in the chambered slides. Cultures were permeabilized in 0.5% Triton X-100, before blocking in 10% BSA and incubation with primary antibodies against aggregated α-synuclein (MJF-14; rabbit MJFR-14-6-4-2, Abcam, #ab209538, 1:25,000), total α-synuclein (mouse LB509, Abcam, #ab27766, 1:500), and neuronal βIII-tubulin (chicken TUJ1, LS Bio, #LS-B5225, 1:500) in 5% BSA for 1 h at RT. Unbound antibody was washed off in 1x TBS + 0.05% Tween-20, followed by incubation with appropriate secondary antibodies (anti-rabbit AlexaFluor-488, Invitrogen #A11008, anti-mouse AlexaFluor-568, Invitrogen #A11004, and anti-chicken AlexaFluor-647, Abcam #ab150175) for 1 h at RT. After another round of washing, most of the buffer was removed, plastic wells broken off the slides, and silicone gasket was removed with a pair of forceps to allow mounting with DAKO fluorescent mounting medium (DAKO, #S3023). After leaving slides to dry, edges were sealed with nail polish.

Immunohistochemistry (IHC)

Before staining, all sections were deparaffinized and rehydrated with series of xylene and gradient ethanol. For IHC on human brain, the antigen was unmasked by 70% (vol/vol) formic acid (Sigma, #F0507-1L), followed by heat induced antigen retrieval in a programmable antigen retrieval cooker (Aptum Bio Retriever 2100) using 1X R-UNIVERSAL Epitope Recovery Buffer (EMS, #62719-10). The sections were then blocked with BLOXALL® Endogenous Alkaline Phosphatase Blocking Solution (VectorLabs, #SP-6000) followed by 5% horse serum before incubation with the primary antibody MJF-14 (anti-conformation-specific α-synuclein filament antibody MJFR-14-6-4-2, Abcam, #ab209538, 1:200). The immunohistology signals were visualised with ImmPRESS®-AP Horse Anti-Rabbit IgG Polymer (VectorLabs, #MP-5401) and ImmPACT™ Vector®Red Alkaline Phosphatase Substrate (VectorLabs, #SK-5105) as per manufacturer's instruction. After counterstaining with cresyl violet, sections were coverslipped with DPX mounting medium (Sigma, #06522).

For IHC on mouse brain, staining was performed in parallel with MJF-14 PLA with identical steps for epitope retrieval, permeabilization, and blocking of endogenous peroxidases. Sections were blocked in 5% normal goat serum (NGS) in PBS before incubation with the primary antibody MJF-14 (anti-conformation-specific α-synuclein filament antibody MJFR-14-6-4-2, Abcam, #ab209538, 1:25,000), overnight at 4 °C. Biotinylated goat anti-rabbit IgG (VectorLabs, #BA-1000-1.5, 1:200) in 2.5% NGS was applied for 1 h at RT, followed by Vectastain® Elite® ABC-HRP kit (VectorLabs, #PK-6100) for 30 min at RT. Staining was visualised with 3,3′-diaminobenzidine (DAB; Sigma, #D5637) for 10 min at RT, and sections were counterstained with nuclear stain from Navinci PLA kit (Navinci, #NB.MR.HRP.100). Samples were left under running tap water for 10 min before rapid dehydration in 100% isopropanol and mounting with VectaMount Express Mounting Medium (Vector Laboratories, #H-5700).

ONE microscopy of PLA

To apply one-step nanoscale expansion (ONE) microscopy imaging[74] to MJF-14 PLA, the PLA protocol was modified slightly to accommodate the specific needs related to staining intensity for the expansion protocol and run with the custom-made PLA detection kit from Navinci, allowing fluorescent labelling of the PLA product using biotin. FFPE sections mounted on glass slides were treated as described above regarding deparaffinization, rehydration, epitope retrieval, permeabilization and PLA blocking steps. Then, a 2-step biotin blocking following manufacturer's instructions (Ready Probes Biotin Blocking Solution (Invitrogen, #R37628) was included, before incubation with conjugated primary antibodies overnight. Naveni Reaction 1 (ligation) and Reaction 2 (amplification) were

performed as indicated in Table 2. Excess reaction reagents were washed off in 1x TBS, followed by 0.1x TBS, as per manufacturer's instructions, then washed in PBS, before autofluorescence quenching in 1x TrueBlack (Biotium, #23007) as described above.

Samples were blocked again, this time in 2.5% BSA + 2.5% NGS + 2.5% normal donkey serum (NDS) in PBS. This was followed by incubation with primary antibodies for immunofluorescence: guineapig VGLUT1 (Synaptic Systems, #135304, 1:200) and Star635P-conjugated α-synuclein nanobody[75] (NbSyn2-St635P, Nanotag custom-made, 10 μM, 1:150) for 1.5 h at RT. Unbound antibody was washed off with 1% BSA + 1% NGS + 1% NDS in PBS, before incubation with appropriate secondary antibodies (streptavidin-AlexaFluor-488 (Invitrogen, #S32354, 1:200) and donkey anti-guineapig Cy3 (Dianova, #706-165-148, 1:200) for 1.5 h at RT. After another three washes in 1% BSA + 1% NGS + 1% NDS in PBS, samples were washed twice in PBS. A third of each sample was then mounted in Mowiol as a non-expanded staining control, while the rest was processed for tissue expansion.

Expansion protocol was performed as described in ref. 124 but with 0.3 mg/mL Acryloyl-X (Invitrogen, #A20770) in MES buffer (N-(morpholino)ethane sulfonic acid-based saline solution, 19.52 mg/mL MES + 87.66 mg/mL NaCl, pH 6). The lower pH enhances the penetration depth of the anchor[125]. Samples were incubated with Acryloyl-X in MES overnight at 4 °C, protected from light. Gelation solution, containing N,N-dimethylacrylamide (DMAA), sodium acrylate, potassium persulfate, and N,N,N′,N′-Tetramethylethylendiamine (TEMED), was mixed and purged with N_2 as previously described[124,126]. A gelation chamber, inspired by Truckenbrodt et al.[126], was created in a 15-cm TC dish, covered with tinfoil and placed upside down. Two stacks of two square coverslips each were affixed to a piece of parafilm, with 20 mm space in-between, using a little bit of nail polish. Once slightly dried, the parafilm/coverslips were flipped upside-down to stick it inside the lid of the TC dish, pressing down the parafilm and letting it dry completely. Finally, gelation chamber was covered with wet tissues along the edges. Gelation solution (~200 μL/slide) was then added in the parafilm-covered space between the coverslips, and slides with tissue sections were placed upside-down on top, edges resting on the coverslips. If necessary, extra gelation solution was pipetted in from the side to ensure coverage of the tissue, before the gelation chamber was closed, and gels left to polymerise overnight at 23 °C (14–18 h).

Next day, gels were washed 5 × 30 min in disruption buffer (100 mM Tris, 5% Triton X-100, 1% SDS, pH 8) and then autoclaved in fresh disruption buffer in a cold-start autoclave on a 30-min programme at 110–121 °C. After allowing the gels to cool down slowly in the autoclave, the samples, which normally detach from their coverslips during either disruption buffer washing or autoclaving, were still attached to the glass slides. Thus, tissue was scraped off the glass slides using a razor blade before proceeding to the expansion step. Then, gels were transferred to 22 × 22 cm culture dishes and ~400 mL ddH$_2$O added to each dish. Water was exchanged twice immediately and then every 30–45 min until gels were fully expanded. Gels were left overnight in ddH$_2$O before imaging.

Imaging and quantification

Cells and human neurons. Samples were imaged on a Zeiss AxioObserver 7 inverted fluorescent microscope with the Zen Blue 2.3 software and 20-30 images were taken per coverslip/well at X63 magnification, using DAPI and tubulin staining as a guidance for the presence of cells. PLA particles were quantified within tubulin-labelled cells, then normalised to the number of cells using Fiji (Fiji Is Just ImageJ, version 2.3.0/1.53t, National Institutes of Health[127]). A minimum of 260 cells were analysed per condition per replicate.

Human DLB cohort. Samples were imaged at X63 magnification on a Zeiss AxioObserver 7 inverted fluorescent microscope with the Zen Blue 2.3 software. For total PLA analysis in DLB and control cases, 20 images were taken randomly per sample, exported as TIFF, background

subtracted, PLA particles counted, and total PLA area computed in Fiji. PLA particle area was averaged per image.

To evaluate PLA signal in LB-positive and LB-negative neurons, large neurons were manually defined from the DAPI-staining, using nucleus size and morphology as guidance (see supplementary Fig. 5 for examples). From merged images, each neuron was then outlined and the original grey-scale PLA-channel TIFF was duplicated for each neuron. Neurons were categorised as either LB-positive (a LB in close proximity to a large neuronal nucleus) or LB-negative (no LB in close proximity). LBs without obvious association to a neuronal nucleus were not included in analysis. PLA images were then filtered using Gaussian blur (sigma = 2) and thresholded using the RenyiEntropy method (threshold = 350). Signals above threshold and larger than 10 pixels^2 (corresponding to a minimum diameter of approx. 250 nm) were counted as PLA and total area of PLA for each neuron was computed. For each image, the PLA area/neuron was averaged between LB-positive and LB-negative neurons to allow a pairwise comparison of PLA area in LB-positive neurons compared to neighbouring (i.e., in the same image) LB-negative neurons.

Human ACC cohort. All PLA- and IHC-labelled sections were autoscanned at X40 on an Olympus VS120 Slide Scanner at the same settings. Orientation was adjusted using the VS-DESKTOP software (Olympus Soft Imaging Solutions GmbH, ver. 2.9 13753) to allow digital images to be cropped at the comparable anatomical locations with similarly sized regions of interest (OlyVIA 3.3; length × width: 510 μm × 495 μm, providing an area of 252,450 μm^2). To assess whether PLA and IHC revealed similar or distinct pathological information, the laminar distribution of PLA positive signals and IHC-revealed α-synuclein deposit particles were quantified for both superficial grey matter (SGM, containing cortical layers I–III) and deep grey matter (DGM, containing cortical layers V–VI). The cropped OlyVIA VSI files were converted into full resolution TIFF files with Fiji for quantification to be completed by researchers blinded to the group sources of cases.

For the quantification of PLA-positive signal, we initially developed a classifier to automatically segment the images into their components (PLA signal, nuclei, and extranuclear area) using the Trainable Weka Segmentation plugin in Fiji[68], based on an optimisation cohort consisting of 6 images. To minimise quantification variability from artificial effects (e.g., colour development), images were categorised into intensely and weakly stained depending on the counterstain intensity of haematoxylin (Supplementary Fig. 3a, b), allowing a separate classifier suitable for nuclei segmentation in each group. Classifier performance was evaluated by the measures sensitivity, precision, and accuracy (see Supplementary Fig. 3) and optimised for sensitivity, i.e., as high detection of the neuronal nuclei as possible. PLA signal segmentation was identical for intensely and weakly stained groups.

For subsequent analyses, images were automatically segmented into PLA signals, nuclei, and extranuclear area, after which PLA signals and nuclei were defined from the probability maps. To distinguish neuronal nuclei from those of glia, a minimum size of 350 pixel (36.7 μm^2, corresponding to an approx. minimum diameter of 7 μm) was set for neuronal nuclei. Total PLA particles were then computed in the entire image, in the neuronal cell bodies (i.e., inside neuronal nuclei and within 3.5 μm radius of nuclei), and in the neuropil (including any signal in glial nuclei) and normalised to either the corresponding tissue area or the neuronal number.

For individual neuronal PLA analyses, neurons were analysed one at a time, and the PLA particles were computed inside the nucleus and in the assumed cytoplasmic region (within a 3.5 μm distance from the nucleus). Then, the neuron was assigned to one of nine semi-quantitative groups. The entire analysis workflow is outlined in Supplementary Fig. 4.

For IHC, the images were quantified for total α-synuclein deposit particles (particles with a minimum length of 2 μm and intensity >50 above background) and LBs (compact round or oval inclusions, sometimes with a halo, with a diameter >5 μm). For the deposit particles, images were colour split with "colour deconvolution" using vectors "H&E 2"[128,129]. MJF-14

signal at colour 2 was then counted using the Cell Counter plugin in Fiji with brightness and contrast slightly adjusted. Any oval or round particle with the longest axis >2 μm and an intensity >50 above the background was defined as a deposit particle in this analysis. LBs were counted manually and confirmed independently by two researchers.

Expansion PLA. Confocal imaging of non-expanded staining control samples was done on an Abberior Expert line setup (Abberior Instruments) with an IX83 microscope (Olympus) and a 100 × oil immersion objective (UPLSAPO, 1.4 NA; Olympus). Excitation lines of 485 nm, 561 nm, and 640 nm were used for AlexaFluor-488, Cy3, and Star635P, respectively. ONE microscopy imaging was carried out on TCS SP5 STED microscope (Leica Microsystems, Wetzlar, Germany) as described previously[74]. Briefly, using a resonant scanner at a speed of 8 kHz, 1500 or 2000 frames of images were taken in uni-directional *xyct* line scans using 633, 561, and 488 nm excitation lines filtered through acousto-optical tunable filters and detected HyD detectors. Each *xyct* image stack was acquired at an 8-bit depth with a pixel size of slightly less of 98 nm, and a format of 128 × 128 pixels. Image acquisitions were imported into the ONE plugin in Fiji to obtain the super-resolved images.

Mouse cohort. Entire X40 slide scans of coronal sections were obtained on an Olympus VS120 Slide Scanner with the VS-ASW imaging software. Image files in the VSI format were opened in QuPath v.0.3.2[130] and regions for comparison were selected. Somatosensory cortex and hippocampus ROIs were selected around bregma −2.055 mm (range −1.755 to −2.355 mm), while midbrain ROIs were selected in the vicinity of the red nucleus, approx. bregma −3.455 mm (range −3.18 to −3.68 mm), based on the Allen mouse brain atlas[131]. No analysis was performed.

Statistics

All data were checked for normality using the Shapiro-Wilks test, and appropriate tests were selected based on normality as well as the number of groups to compare. In cell experiments, groups were compared using a Kruskal-Wallis one-way ANOVA followed by the Dunn post hoc test to account for multiple comparisons, as not all groups were normally distributed. For human cortical neurons, groups were compared using a two-way ANOVA followed by Tukey's multiple comparison test, with treatment as one grouping variable and technical replicate no. as the other grouping variable. For comparison of PLA particles in DLB and control brain sections, groups were compared using a Mann–Whitney U-test (total PLA/image) or a Wilcoxon matched-pairs signed rank test (PLA in LB-positive and LB-negative neurons) as data did not pass the test for normality. All statistics were two-tailed, performed in GraphPad Prism 9, with the exception of the human ACC data.

For the human ACC, all statistical analyses were performed using the SPSS software (IBM, ver. 26). Differences between all groups in demographic variables (Table 1) were assessed using one-way ANOVA (age and post-mortem delay), Pearson chi-square (gender), and Student's T-test for disease duration between PD groups. Two-factor univariate analyses (group by region) were used to assess whether there were any regional differences in the PLA signals quantified in the ACC of the different groups, covarying for age, post-mortem delay, and gender, followed by post hoc Bonferroni tests. A Spearman's rho correlation was performed to identify significant associations between PLA density in neuronal and neuropil compartments, between the densities of PLA signals and IHC-revealed deposit particles, and between deposit particles and LBs specifically. For correlation between deposit particles and LBs, cases with no LBs in an ROI were excluded. To determine if the distribution of PLA signals varied within the neurons of the different groups, univariate analyses of the PLA levels in the neurons (nucleus, cytoplasm, and both) as well as outside the neuronal somas (in the neuropil) were performed, covarying for age, post-mortem delay, and gender, and again post hoc Bonferroni tests were used to identify any significant group differences.

All data are displayed as mean ± standard error of the mean (SEM), unless otherwise stated, and p-values are indicated as *$p < 0.05$, **$p < 0.01$, ***$p < 0.001$, ****$p < 0.0001$. Graphs were generated in GraphPad Prism 9, while figures were created using Adobe Illustrator and BioRender (Publication license agreement UF26YL0C58).

Data availability
The datasets used and/or analysed during the current study available from the corresponding author on reasonable request.

Code availability
Fiji macro scripts used for quantifications are available upon request to the corresponding author.

References
1. Spillantini, M. G. & Goedert, M. The α-synucleinopathies: Parkinson's disease, dementia with Lewy bodies, and multiple system atrophy. *Ann. N. Y. Acad. Sci.* **920**, 16–27 (2000).
2. de Lau, L. M. L. et al. Epidemiology of Parkinson's disease. *Lancet Neurol.* **5**, 525–535 (2006).
3. Ascherio, A. & Schwarzschild, M. A. The epidemiology of Parkinson's disease: risk factors and prevention. *Lancet Neurol.* **15**, 1257–1272 (2016).
4. Polymeropoulos, M. H. Mutation in the α-Synuclein gene identified in families with Parkinson's disease. *Science* **276**, 2045–2047 (1997).
5. Krüger, R. et al. Ala30Pro mutation in the gene encoding α-synuclein in Parkinson's disease. *Nat. Genet.* **18**, 106–108 (1998).
6. Singleton, A. B. et al. Synuclein locus triplication causes Parkinson's disease. *Science* **302**, 841 (2003).
7. Chartier-Harlin, M. C. et al. synuclein locus duplication as a cause of familial Parkinson's disease. *Lancet* **364**, 1167–1169 (2004).
8. Zarranz, J. J. et al. The new mutation, E46K, of α-Synuclein Causes Parkinson and lewy body dementia. *Ann. Neurol.* **55**, 164–173 (2004).
9. Konno, T., Ross, O. A., Puschmann, A., Dickson, D. W. & Wszolek, Z. K. Autosomal dominant Parkinson's disease caused by SNCA duplications. *Parkinsonism Relat. Disord.* **22**, S1–S6 (2016).
10. Wood, S. J. et al. Synuclein Fibrillogenesis is nucleation-dependent. *J. Biol. Chem.* **274**, 19509–19512 (2002).
11. Wakabayashi, K., Tanji, K., Mori, F. & Takahashi, H. The Lewy body in Parkinson's disease: molecules implicated in the formation and degradation of α-synuclein aggregates. *Neuropathology* **27**, 494–506 (2007).
12. Flagmeier, P. et al. Mutations associated with familial Parkinson's disease alter the initiation and amplification steps of α-synuclein aggregation. *Proc. Natl Acad. Sci. USA* **113**, 10328–10333 (2016).
13. Angot, E., Steiner, J. A., Hansen, C., Li, J. Y. & Brundin, P. Are synucleinopathies prion-like disorders? *Lancet Neurol.* **9**, 1128–1138 (2010).
14. Masuda-Suzukake, M. et al. Prion-like spreading of pathological α-synuclein in brain. *Brain* **136**, 1128–1138 (2013).
15. Prusiner, S. B. et al. Evidence for α-synuclein prions causing multiple system atrophy in humans with parkinsonism. *Proc. Natl Acad. Sci. USA* https://doi.org/10.1073/pnas.1514475112 (2015).
16. Brundin, P. & Melki, R. Prying into the prion hypothesis for parkinson's disease. *J. Neurosci.* **37**, 9808–9818 (2017).
17. Braak, H. et al. Staging of brain pathology related to sporadic Parkinson's disease. *Neurobiol. Aging* **24**, 197–211 (2003).
18. Braak, H., Ghebremedhin, E., Rüb, U., Bratzke, H. & Del Tredici, K. Stages in the development of Parkinson's disease-related pathology. *Cell Tissue Res.* **318**, 121–134 (2004).
19. Terry, R. D. Do neuronal inclusions kill the cell? *Adv. Dementia Res.* 91–93, https://doi.org/10.1007/978-3-7091-6781-6_12. (2000).
20. Olanow, C. W., Perl, D. P., DeMartino, G. N. & McNaught, K. S. P. Lewy-body formation is an aggresome-related process: a hypothesis. *Lancet Neurol* **3**, 496–503 (2004).
21. Parkkinen, L., Kauppinen, T., Pirttilä, T., Autere, J. M. & Alafuzoff, I. α-synuclein pathology does not predict extrapyramidal symptoms or dementia. *Ann. Neurol.* **57**, 82–91 (2005).
22. Parkkinen, L. et al. Disentangling the relationship between lewy bodies and nigral neuronal loss in Parkinson's disease. *J. Parkinsons Dis.* **1**, 277–286 (2011).
23. Chartier, S. & Duyckaerts, C. Is Lewy pathology in the human nervous system chiefly an indicator of neuronal protection or of toxicity? *Cell Tissue Res.* **373**, 1–12 (2018).
24. Volles, M. J. et al. Vesicle permeabilization by protofibrillar α-synuclein: Implications for the pathogenesis and treatment of Parkinson's disease. *Biochemistry* **40**, 7812–7819 (2001).
25. Caughey, B. & Lansbury, P. T. Protofibrils, pores, fibrils, and neurodegeneration: separating the responsible protein aggregates from the innocent bystanders. *Annu. Rev. Neurosci.* **26**, 267–298 (2003).
26. Apetri, M. M., Maiti, N. C., Zagorski, M. G., Carey, P. R. & Anderson, V. E. Secondary structure of alpha-synuclein oligomers: characterization by raman and atomic force microscopy. *J. Mol. Biol.* **355**, 63–71 (2006).
27. Danzer, K. M., Krebs, S. K., Wolff, M., Birk, G. & Hengerer, B. Seeding induced by alpha-synuclein oligomers provides evidence for spreading of alpha-synuclein pathology. *J. Neurochem.* **111**, 192–203 (2009).
28. Celej, M. S. et al. Toxic prefibrillar α-synuclein amyloid oligomers adopt a distinctive antiparallel β-sheet structure. *Biochem J.* **443**, 719–726 (2012).
29. Cremades, N. et al. Direct observation of the interconversion of normal and toxic forms of α-synuclein. *Cell* **149**, 1048–1059 (2012).
30. Danzer, K. M. et al. Exosomal cell-to-cell transmission of alpha synuclein oligomers. *Mol. Neurodegener.* **7**, 1–18 (2012).
31. Pieri, L., Madiona, K. & Melki, R. Structural and functional properties of prefibrillar α-synuclein oligomers. *Sci. Rep.* **6**, 1–15 (2016).
32. Bengoa-Vergniory, N., Roberts, R. F., Wade-Martins, R. & Alegre-Abarrategui, J. Alpha-synuclein oligomers: a new hope. *Acta Neuropathol.* **134**, 819–838 (2017).
33. Cascella, R. et al. The release of toxic oligomers from α-synuclein fibrils induces dysfunction in neuronal cells. *Nat. Commun.* **12**, 1–16 (2021).
34. Winner, B. et al. In vivo demonstration that α-synuclein oligomers are toxic. *Proc. Natl Acad. Sci. USA* **108**, 4194–4199 (2011).
35. Fusco, G. et al. Structural basis of membrane disruption and cellular toxicity by α-synuclein oligomers. *Science* **358**, 1440–1443 (2017).
36. Prots, I. et al. Synuclein oligomers induce early axonal dysfunction in human iPSC-based models of synucleinopathies. *Proc. Natl Acad. Sci. USA* **115**, 7813–7818 (2018).
37. Ingelsson, M. Alpha-synuclein oligomers-neurotoxic molecules in Parkinson's disease and other lewy body disorders. *Front. Neurosci.* **10**, 408 (2016).
38. Alam, P., Bousset, L., Melki, R. & Otzen, D. E. α-synuclein oligomers and fibrils: a spectrum of species, a spectrum of toxicities. *J. Neurochem.* **150**, 522–534 (2019).
39. Du, X. Y., Xie, X. X. & Liu, R. T. The role of α-Synuclein oligomers in Parkinson's Disease. *Int. J. Mol. Sci.* **21**, 8645 (2020).
40. Kayed, R., Dettmer, U. & Lesné, S. E. Soluble endogenous oligomeric α-synuclein species in neurodegenerative diseases: Expression, spreading, and cross-talk. *J. Parkinsons Dis.* **10**, 791–818 (2020).

41. Vaikath, N. N. et al. Generation and characterization of novel conformation-specific monoclonal antibodies for α-synuclein pathology. *Neurobiol. Dis.* **79**, 81–99 (2015).

42. Kumar, S. T. et al. How specific are the conformation-specific α-synuclein antibodies? Characterization and validation of 16 α-synuclein conformation-specific antibodies using well-characterized preparations of α-synuclein monomers, fibrils and oligomers with distinct struct. *Neurobiol. Dis.* **146**, 105086 (2020).

43. Outeiro, T. F. et al. Formation of toxic oligomeric α-synuclein species in living cells. *PLoS ONE* **3**, e1867 (2008).

44. Gonçalves, S. A., Matos, J. E. & Outeiro, T. F. Zooming into protein oligomerization in neurodegeneration using BiFC. *Trends Biochem. Sci.* **35**, 643–651 (2010).

45. Fredriksson, S. et al. Protein detection using proximity-dependent DNA ligation assays. *Nat. Biotechnol.* **20**, 473–477 (2002).

46. Roberts, R. F., Wade-Martins, R. & Alegre-Abarrategui, J. Direct visualization of alpha-synuclein oligomers reveals previously undetected pathology in Parkinson's disease brain. *Brain* **138**, 1642–1657 (2015).

47. Berkhoudt Lassen, L. et al. ELISA method to detect α-synuclein oligomers in cell and animal models. *PLoS ONE* **13**, e0196056 (2018).

48. Ruesink, H. et al. Stabilization of α-synuclein oligomers using formaldehyde. *PLoS ONE* **14**, e0216764 (2019).

49. Vekrellis, K., Xilouri, M., Emmanouilidou, E. & Stefanis, L. Inducible over-expression of wild type α-synuclein in human neuronal cells leads to caspase-dependent non-apoptotic death. *J. Neurochem.* **109**, 1348–1362 (2009).

50. Betzer, C. et al. Alpha-synuclein aggregates activate calcium pump SERCA leading to calcium dysregulation. *EMBO Rep.* **19**, e44617 (2018).

51. El-Agnaf, O. M. A. et al. A strategy for designing inhibitors of α-synuclein aggregation and toxicity as a novel treatment for Parkinson's disease and related disorders. *FASEB J.* **18**, 1315–1317 (2004).

52. Sekiya, H. et al. Wide distribution of alpha-synuclein oligomers in multiple system atrophy brain detected by proximity ligation. *Acta Neuropathol.* **137**, 455–466 (2019).

53. Behere, A. et al. Visualization of early oligomeric α-synuclein pathology and its impact on the dopaminergic system in the (Thy-1)-h[A30P]α-syn transgenic mouse model. *J. Neurosci. Res.* **99**, 2525–2539 (2021).

54. Sekiya, H. et al. Discrepancy between distribution of alpha-synuclein oligomers and Lewy-related pathology in Parkinson's disease. *Acta Neuropathol. Commun.* **10**, 133 (2022).

55. Burré, J., Sharma, M. & Südhof, T. C. α-Synuclein assembles into higher-order multimers upon membrane binding to promote SNARE complex formation. *Proc. Natl Acad. Sci. USA* **111**, E4274–E4283 (2014).

56. Bartels, T., Choi, J. G. & Selkoe, D. J. α-Synuclein occurs physiologically as a helically folded tetramer that resists aggregation. *Nature* **477**, 107–110 (2011).

57. Iyer, A., Schilderink, N., Claessens, M. M. A. E. & Subramaniam, V. Membrane-Bound Alpha Synuclein Clusters induce impaired lipid diffusion and increased lipid packing. *Biophys. J.* **111**, 2440–2449 (2016).

58. Rabe, M. et al. On-surface aggregation of α-synuclein at nanomolar concentrations results in two distinct growth mechanisms. *ACS Chem. Neurosci.* **4**, 408–417 (2013).

59. Volpicelli-Daley, L. A. et al. Exogenous α-Synuclein fibrils induce lewy body pathology leading to synaptic dysfunction and neuron death. *Neuron* **72**, 57–71 (2011).

60. Liekniņa, I. et al. Structural basis of epitope recognition by anti-alpha-synuclein antibodies MJFR14-6-4-2. *npj Parkinsons Dis.* **10**, 206 (2024).

61. Li, W. et al. Aggregation promoting C-terminal truncation of α-synuclein is a normal cellular process and is enhanced by the familial Parkinson's disease-linked mutations. *Proc. Natl Acad. Sci. USA* **102**, 2162–2167 (2005).

62. Karpowicz, R. J. et al. Selective imaging of internalized proteopathic α-synuclein seeds in primary neurons reveals mechanistic insight into transmission of synucleinopathies. *J. Biol. Chem.* **292**, 13482–13497 (2017).

63. Mahul-Mellier, A. L. et al. The process of Lewy body formation, rather than simply α-synuclein fibrillization, is one of the major drivers of neurodegeneration. *Proc. Natl Acad. Sci. USA* **117**, 4971–4982 (2020).

64. Elfarrash, S. et al. Organotypic slice culture model demonstrates inter-neuronal spreading of alpha-synuclein aggregates. *Acta Neuropathol. Commun.* **7**, 213 (2019).

65. Gray, D. A. & Woulfe, J. Lipofuscin and aging: a matter of toxic waste. *Sci. Aging Knowledge Environ.* **2005**, re1 (2005).

66. Ottis, P. et al. Human and rat brain lipofuscin proteome. *Proteomics* **12**, 2445–2454 (2012).

67. Murphy, K. E. et al. Reduced glucocerebrosidase is associated with increased α-synuclein in sporadic Parkinson's disease. *Brain* **137**, 834–848 (2014).

68. Arganda-Carreras, I. et al. Trainable Weka Segmentation: a machine learning tool for microscopy pixel classification. *Bioinformatics* **33**, 2424–2426 (2017).

69. Harding, A. J. & Halliday, G. M. Cortical Lewy body pathology in the diagnosis of dementia. *Acta Neuropathol.* **102**, 355–363 (2001).

70. Schulz-Schaeffer, W. J. The synaptic pathology of α-synuclein aggregation in dementia with Lewy bodies, Parkinson's disease and Parkinson's disease dementia. *Acta Neuropathol.* **120**, 131–143 (2010).

71. Nakata, Y. et al. Accumulation of α-Synuclein triggered by presynaptic dysfunction. *J. Neurosci.* **32**, 17186–17196 (2012).

72. Colom-Cadena, M. et al. Synaptic phosphorylated α-synuclein in dementia with Lewy bodies. *Brain* **140**, 3204–3214 (2017).

73. Awa, S. et al. Phosphorylation of endogenous α-synuclein induced by extracellular seeds initiates at the pre-synaptic region and spreads to the cell body. *Sci. Rep.* **12**, 1–13 (2022).

74. Shaib, A. H. et al. One-step nanoscale expansion microscopy reveals individual protein shapes. *Nat Biotechnol.* 1-9 (2024).

75. De Genst, E. J. et al. Structure and properties of a complex of α-Synuclein and a single-domain camelid antibody. *J. Mol. Biol.* **402**, 326–343 (2010).

76. Peters, A. & Harriman, K. M. Different kinds of axon terminals forming symmetric synapses with the cell bodies and initial axon segments of layer II/III pyramidal cells. I. Morphometric analysis. *J. Neurocytol.* **19**, 154–174 (1990).

77. Mitchell, N. et al. Sonic hedgehog regulates presynaptic terminal size, ultrastructure and function in hippocampal neurons. *J. Cell Sci.* **125**, 4207–4213 (2012).

78. Nosov, G., Kahms, M. & Klingauf, J. The decade of super-resolution microscopy of the presynapse. *Front. Synaptic Neurosci.* **12**, 32 (2020).

79. Wilhelm, B. G. et al. Composition of isolated synaptic boutons reveals the amounts of vesicle trafficking proteins. *Science* **344**, 1023–1028 (2014).

80. Moore, R. P. & Legant, W. R. Improving probes for super-resolution. *Nat. Methods* **15**, 659–660 (2018).

81. Lavedan, C. The synuclein family. *Genome Res.* **8**, 871–880 (1998).

82. Ferreira, N. et al. Multiple system atrophy-associated oligodendroglial protein p25α stimulates formation of novel α-synuclein strain with enhanced neurodegenerative potential. *Acta Neuropathol.* **142**, 87–115 (2021).

83. Ferreira, S. A. et al. Sex-dimorphic neuroprotective effect of CD163 in an α-synuclein mouse model of Parkinson's disease. *npj Parkinson's Dis.* **9**, 1–21 (2023).

84. Ishimoto, T. et al. A novel mouse model for investigating α-synuclein aggregates in oligodendrocytes: implications for the glial cytoplasmic inclusions in multiple system atrophy. *Mol. Brain* **17**, 1–13 (2024).

85. Estaun-Panzano, J., Arotcarena, M. L. & Bezard, E. Monitoring α-synuclein aggregation. *Neurobiol. Dis.* **176**, 105966 (2023).

86. Kalaitzakis, M. E., Graeber, M. B., Gentleman, S. M. & Pearce, R. K. B. The dorsal motor nucleus of the vagus is not an obligatory trigger site of Parkinson's disease: a critical analysis of α-synuclein staging. *Neuropathol. Appl Neurobiol.* **34**, 284–295 (2008).

87. Parkkinen, L., Pirttilä, T. & Alafuzoff, I. Applicability of current staging/categorization of α-synuclein pathology and their clinical relevance. *Acta Neuropathol.* **115**, 399–407 (2008).

88. Zaccai, J., Brayne, C., McKeith, I., Matthews, F. & Ince, P. G. Patterns and stages of α-synucleinopathy. *Neurology* **70**, 1042–1048 (2008).

89. Altay, M. F., Liu, A. K. L., Holton, J. L., Parkkinen, L. & Lashuel, H. A. Prominent astrocytic alpha-synuclein pathology with unique post-translational modification signatures unveiled across Lewy body disorders. *Acta Neuropathol. Commun.* **10**, 1–18 (2022).

90. Borghammer, P. & Van Den Berge, N. Brain-First versus Gut-First Parkinson's Disease: a hypothesis. *J. Parkinson's Dis.* **9**, S281–S295 (2019).

91. Horsager, J. et al. Brain-first versus body-first Parkinson's disease: a multimodal imaging case-control study. *Brain* **143**, 3077–3088 (2020).

92. Borghammer, P. et al. Neuropathological evidence of body-first vs. brain-first Lewy body disease. *Neurobiol. Dis.* **161**, 105557 (2021).

93. Knudsen, K. et al. Asymmetric Dopaminergic dysfunction in brain-first versus body-first Parkinson's Disease Subtypes. *J. Parkinsons Dis.* **11**, 1677–1687 (2021).

94. Greffard, S. et al. A stable proportion of Lewy body bearing neurons in the substantia nigra suggests a model in which the Lewy body causes neuronal death. *Neurobiol. Aging* **31**, 99–103 (2010).

95. Osterberg, V. R. et al. Progressive aggregation of alpha-synuclein and selective degeneration of lewy inclusion-bearing neurons in a mouse model of Parkinsonism. *Cell Rep.* **10**, 1252–1260 (2015).

96. Huang, Z., Xu, Z., Wu, Y. & Zhou, Y. Determining nuclear localization of alpha-synuclein in mouse brains. *Neuroscience* **199**, 318–332 (2011).

97. Rutherford, N. J., Brooks, M. & Giasson, B. I. Novel antibodies to phosphorylated α-synuclein serine 129 and NFL serine 473 demonstrate the close molecular homology of these epitopes. *Acta Neuropathol. Commun.* **4**, 80 (2016).

98. Lin, W. L., Delucia, M. W. & Dickson, D. W. α-Synuclein immunoreactivity in neuronal nuclear inclusions and neurites in multiple system atrophy. *Neurosci. Lett.* **354**, 99–102 (2004).

99. Nishie, M., Mori, F., Yoshimoto, M., Takahashi, H. & Wakabayashi, K. A quantitative investigation of neuronal cytoplasmic and intranuclear inclusions in the pontine and inferior olivary nuclei in multiple system atrophy. *Neuropathol. Appl Neurobiol.* **30**, 546–554 (2004).

100. Weston, L. J. et al. Aggregated Alpha-Synuclein inclusions within the nucleus predict impending neuronal cell death in a mouse model of Parkinsonism. *Int. J. Mol. Sci.* **23**, 15294 (2022).

101. Schaser, A. J. et al. Alpha-synuclein is a DNA binding protein that modulates DNA repair with implications for Lewy body disorders. *Sci. Rep.* **9**, 10919 (2019).

102. Pinho, R. et al. Nuclear localization and phosphorylation modulate pathological effects of alpha-synuclein. *Hum. Mol. Genet.* **28**, 31–50 (2019).

103. Pan, Y. et al. Nuclear localization of alpha-synuclein affects the cognitive and motor behavior of mice by inducing DNA damage and abnormal cell cycle of hippocampal neurons. *Front. Mol. Neurosci.* **15**, 1015881 (2022).

104. Ho, D. H., Kim, H., Nam, D., Heo, J. & Son, I. Nuclear α-Synuclein-Derived cytotoxic effect via altered ribosomal RNA processing in primary mouse embryonic fibroblasts. *Int. J. Mol. Sci.* **24**, 2132 (2023).

105. Du, T. et al. Nuclear alpha-synuclein accelerates cell senescence and neurodegeneration. *Immun. Ageing* **21**, 1–16 (2024).

106. Pan, Y. et al. Nuclear localization of alpha-synuclein induces anxiety-like behavior in mice by decreasing hippocampal neurogenesis and pathologically affecting amygdala circuits. *Neurosci. Lett.* **816**, 137490 (2023).

107. Koss, D. J. et al. Nuclear alpha-synuclein is present in the human brain and is modified in dementia with Lewy bodies. *Acta Neuropathol. Commun.* **10**, 98 (2022).

108. Hegazy, M. et al. Proximity ligation assay for detecting protein-protein interactions and protein modifications in cells and tissues in situ. *Curr. Protoc. Cell Biol.* **89**, e115 (2020).

109. Law, A. M. K. et al. Andy's Algorithms: new automated digital image analysis pipelines for FIJI. *Sci. Rep.* **7**, 1–11 (2017).

110. López-Cano, M., Fernández-Dueñas, V. & Ciruela, F. Proximity ligation assay image analysis protocol: Addressing receptor-receptor interactions. *Methods Mol. Biol.* **2040**, 41–50 (2019).

111. Debaize, L., Jakobczyk, H., Rio, A. G., Gandemer, V. & Troadec, M. B. Optimization of proximity ligation assay (PLA) for detection of protein interactions and fusion proteins in non-adherent cells: application to pre-B lymphocytes. *Mol. Cytogenet* **10**, 1–13 (2017).

112. Lövestam, S. et al. Seeded assembly in vitro does not replicate the structures of α-synuclein filaments from multiple system atrophy. *FEBS Open Bio* **11**, 999–1013 (2021).

113. Lee, S. S., Civitelli, L. & Parkkinen, L. Brain-derived and in vitro-seeded alpha-synuclein fibrils exhibit distinct biophysical profiles. *Elife* **13**, RP92775 (2024).

114. Lindersson, E. et al. Proteasomal Inhibition by α-Synuclein Filaments and Oligomers. *J. Biol. Chem.* **279**, 12924–12934 (2004).

115. Ferreira, N. et al. Trans-synaptic spreading of alpha-synuclein pathology through sensory afferents leads to sensory nerve degeneration and neuropathic pain. *Acta Neuropathol. Commun.* **9**, 1–17 (2021).

116. Ferreira, N. et al. Prodromal neuroinvasion of pathological α-synuclein in brainstem reticular nuclei and white matter lesions in a model of α-synucleinopathy. *Brain Commun.* **3**, fcab104 (2021).

117. Shi, Y., Kirwan, P., Smith, J., Robinson, H. P. C. & Livesey, F. J. Human cerebral cortex development from pluripotent stem cells to functional excitatory synapses. *Nat. Neurosci.* **15**, 477–486 (2012).

118. Gantner, C. W. et al. FGF-MAPK signaling regulates human deep-layer corticogenesis. *Stem Cell Rep.* **16**, 1262–1275 (2021).

119. Rockenstein, E. et al. Differential neuropathological alterations in transgenic mice expressing α-synuclein from the platelet-derived growth factor and Thy-1 promoters. *J. Neurosci. Res.* https://doi.org/10.1002/jnr.10231. (2002).

120. Baptista, M. A. S. et al. A strategy for the generation, characterization and distribution of animal models by the Michael J. Fox Foundation for Parkinson's Research. *Dis. Models Mech.* **6**, 1316–1324 (2013).

121. Ninkina, N. et al. A novel resource for studying function and dysfunction of α-synuclein: mouse lines for modulation of endogenous Snca gene expression. *Sci. Rep.* **5**, 1–6 (2015).

122. Goloborshcheva, V. V., Chaprov, K. D., Teterina, E. V., Ovchinnikov, R. & Buchman, V. L. Reduced complement of dopaminergic neurons in the substantia nigra pars compacta of mice with a constitutive 'low footprint' genetic knockout of alpha-synuclein. *Mol. Brain* **13**, 1–4 (2020).

123. Connor-Robson, N., Peters, O. M., Millership, S., Ninkina, N. & Buchman, V. L. Combinational losses of synucleins reveal their differential requirements for compensating age-dependent

alterations in motor behavior and dopamine metabolism. *Neurobiol. Aging* **46**, 107–112 (2016).

124. Saal, K. A. et al. Heat denaturation enables multicolor X10-STED microscopy. *Sci. Rep.* **13**, 1–15 (2023).

125. Tillberg, P. W. et al. Protein-retention expansion microscopy of cells and tissues labeled using standard fluorescent proteins and antibodies. *Nat. Biotechnol.* **34**, 987–992 (2016).

126. Truckenbrodt, S., Sommer, C., Rizzoli, S. O. & Danzl, J. G. A practical guide to optimization in X10 expansion microscopy. *Nat. Protoc.* **14**, 832–863 (2019).

127. Schindelin, J. et al. Fiji: an open-source platform for biological-image analysis. *Nat. Methods* **9**, 676–682 (2012).

128. Ruifrok, A. C. & Johnston, D. A. Quantification of histochemical staining by color deconvolution. *Anal. Quant. Cytol. Histol.* **23**, 291–299 (2001).

129. Landini, G., Martinelli, G. & Piccinini, F. Colour deconvolution: stain unmixing in histological imaging. *Bioinformatics* **37**, 1485–1487 (2021).

130. Bankhead, P. et al. QuPath: Open source software for digital pathology image analysis. *Sci. Rep.* **7**, 1–7 (2017).

131. Allen Institute. Allen Brain Atlas: Mouse Brain. http://mouse.brain-map.org/experiment/thumbnails/100142143?image_type=atlas (2008).

Author contributions
N.M.J., Y.F., C.B., G.M.H., and P.H.J. contributed to the conception and design of the study. N.M.J., Y.F., H.L., C.B., S.E., A.H.S., D.K., Z.V., L.R., H.G., and M.D. performed the experiments. Data analysis was performed by N.M.J., Y.F., H.L., C.B., S.E., and G.M.H., while Y.F., A.H.S., V.B., S.O.R., G.M.H., and P.H.J. provided critical input for the interpretation of data. Figures were prepared by N.M.J., Y.F., C.B., S.E., and A.H.S., and N.M.J. wrote the first draft of the manuscript. All authors provided critical feedback and approved the final version of the manuscript.

Competing interests
The authors declare no competing interests.

Additional information
Supplementary information The online version contains supplementary material available at https://doi.org/10.1038/s41531-024-00841-9.

Correspondence and requests for materials should be addressed to Nanna Møller Jensen or Poul Henning Jensen.

Reprints and permissions information is available at http://www.nature.com/reprints

Publisher's note Springer Nature remains neutral with regard to jurisdictional claims in published maps and institutional affiliations.